Master's Thesis

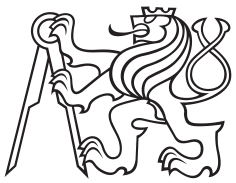

Czech Technical University in Prague

F3

Faculty of Electrical Engineering
Department of Control Engineering

Flow control by shaping electric field through an array of microelectrodes

Jan Machek

January 2017
Supervisor: Doc. Ing. Zdeněk Hurák Ph.D.

Czech Technical University in Prague
Faculty of Electrical Engineering

Department of Control Engineering

DIPLOMA THESIS ASSIGNMENT

Student: **Machek Jan**

Study programme: Cybernetics and Robotics
Specialisation: Systems and Control

Title of Diploma Thesis: **Flow control by shaping electric field through an array of microelectrodes**

Guidelines:

The ultimate goal is to harness electroosmosis as a viable nonmechanical physical phenomenon for programmable driving/actuating/stirring a liquid around over a flat substrate by controlling voltages applied to an array of microelectrodes.

1. Develop a mathematical model of a fluid flow induced by an electric field (electroosmosis) shaped through and array of microelectrodes. Consider several microelectrode layouts. Implement the model in Comsol and simulate it under several scenarios.
2. Design and build (or assign building) a few microfluidic/electrokinetic chips that will be used to demonstrate the modelled phenomena.
3. Conduct a few experiments and compare the results of these experiments and numerical simulations.
4. Design some simple model-based control schemes for such as planar multi-way valves and mixers and demonstrate using experiments.

Bibliography/Sources:

[1] Morgan, Hywel, and Nicolas G. Green. AC electrokinetics: colloids and nanoparticles. Research Studies Press, 2003.
[2] Kirby, Brian J. Micro-and nanoscale fluid mechanics: transport in microfluidic devices. Cambridge University Press, 2010.
[3] Ramos, Antonio, et al. "Pumping of liquids with traveling-wave electroosmosis." Journal of Applied Physics 97.8 (2005): 084906.
[4] Hrdlicka, Jiri, et al. "Mathematical modeling of ac electroosmosis in microfluidic and nanofluidic chips using equilibrium and non-equilibrium approaches." Journal of Applied Electrochemistry 40.5 (2010): 967-980.
[5] Green, Nicolas G., et al. "Fluid flow induced by nonuniform ac electric fields in electrolytes on microelectrodes. I. Experimental measurements." Physical review E 61.4 (2000): 4011.
[6] Gonzalez, Antonio, et al. "Fluid flow induced by nonuniform ac electric fields in electrolytes on microelectrodes. II. A linear double-layer analysis." Physical review E 61.4 (2000): 4019.

Diploma Thesis Supervisor: doc. Ing. Zdeněk Hurák, Ph.D.

Valid until the summer semester 2017/2018

prof. Ing. Michael Šebek, DrSc.
Head of Department

prof. Ing. Pavel Ripka, CSc.
Dean

Prague, November 30, 2016

Acknowledgement / Declaration

First and foremost, I would like to express the sincerest thanks to my thesis supervisor doc. Ing. Zdeněk Hurák, Ph.D. I am very grateful for the opportunity to join his research group AA4CC, for all the advice and ideas he shared with me and for his help and friendly attitude throughout my work on this thesis.

I would also like to thank prof. Ing. Michal Přibyl, Ph.D., for consulting the created mathematical model with me.

Next, I would like to thank Joris More Chevalier, Ph.D., and Ing. Ján Lančok, Ph.D., from Institute of Physics of the Czech Academy of Sciences for helping me with the microelectrode arrays fabrication.

Great Thank you also belongs to all the members of AA4CC research group for all sorts of hints and hacks which helped me especially with the hardware parts of this thesis. Furthermore, I appreciate the friendly atmosphere inside the research group.

Last but not least, this thesis would not have been possible without my family and my girlfriend who have supported me throughout my studies and life.

I declare that I wrote the presented thesis on my own and that I cited all the used information sources in compliance with the Methodical instructions about the ethical principles for writing an academic thesis.

Prague 9. 1. 2017

.....

Abstrakt / Abstract

Tato práce se zabývá využitím jevu zvaného elektroosmóza pro nekontaktní manipulaci s kapalinou a/nebo s mikročásticemi do ni ponořenými. Na rozdíl od dostupných prací se tato práce neomezuje pouze na jednorozměrný pohyb kapaliny v mikrokanálku, nýbrž je uvažován 2D nebo dokonce plný 3D pohyb. Vznik elektroosmózy je v práci vysvětlen, matematicky popsán a následně numericky odsimulován v komerčním řešiči pro metodu konenčných prvků COMSOL Multiphysics. Pro ověření prezentovaného modelu bylo navrhnuto a vyrobeno pět mikroelektrodových polí. Výrobní proces je v práci také popsán. S využitím těchto vyrobených polí byly provedeny experimenty, které byly následně zdokumentovány a diskutovány. V poslední kapitole jsou pak navrženy tři metody řízení pro manipulaci s kapalinou i s částicemi v ní ponořenými. Tyto metody jsou ověřeny na vytvořeném matematickém modelu.

Klíčová slova: Elektrokinetika, mikrofluidika, mikromanipulace, elektroosmóza, dielektroforéza, elektrická dvojitá vrstva, metoda konečných prvků, fotolitografie.

In presented thesis, utilization of a physical phenomenon called electroosmosis for a non-contact fluid flow control and/or micro object manipulation is analyzed. Unlike most of the current state of the art research papers, this thesis does not restrict the considered domain to a one-dimensional microchannel, but two- or even three-dimensional motion is considered. The physical problem itself is explained and a mathematical model is created and numerically simulated in COMSOL Multiphysics, a commercial finite element method solver. Five microelectrode arrays were fabricated and used to perform experiments to validate derived model. The fabrication process is also documented. Then three control approaches to manipulating fluid and a particle immersed in the fluid are proposed in the end of this thesis. The control methods are verified using the mathematical model.

Keywords: Electrokinetics, microfluidics, micromanipulation, electroosmosis, dielectrophoresis, electrical double layer, finite element method, photolithography.

Contents /

Tables / Figures

Chapter 1
Introduction

1.1 Lab-on-chip systems

The continuing technological progress allows us to miniaturize all sorts of objects and instruments. One of the most famous examples is a computer. Machines which used to take up whole lecture halls can now be fitted onto a chip the size of a grain of rice and even smaller. In recent decades the same evolution is happening to the biomedical equipment. Among all the other possible motivations there is also an ambition to insert these small computers with lab-on-chip devices inside a human body, or eventually, if not right inside the body, as easily portable or wearable devices.

The so-called lab-on-chip devices or micro total analysis systems (μTAS) are apparatuses capable of various biological, medical and chemical tasks while having a size in micro or even nanometer scale. Usually, these devices are designed to take care of a single operation over a number of cells or a working liquid solution. The small size makes these systems portable and once designed also cheap to manufacture. Because of these important properties, lab-on-chip systems are convenient one-use diagnosis devices.

1.2 Goal of the thesis

Even though sometimes it is enough to just deposit a drop of patient's blood into a prepared reservoir to make use of a specific μTAS device, often cell actuation and manipulation or fluid pumping is necessary to carry out to complete the device's purpose. Fluid control in such devices is a topic of presented master's thesis. The physical phenomenon used for actuating the liquid is called electroosmosis. The motion is induced by shaping the electric field inside considered domain. Microelectrodes placed underneath the domain would be used to shape the electric field.

The ultimate goal would be not only to drive the fluid itself but also to use it to manipulate microobjects immersed in the fluid.

1.3 Outline of the thesis

The thesis is structured as follows. First, a state-of-the-art research is given. Then the physical nature of electroosmosis is explained. In chapter 4 the reader can find a mathematical model of electroosmosis. To perform various experiments, microelectrode arrays had to be fabricated. Information about this process are in chapter 5. The experiments were carried out and the results and discussion are presented in chapter 6. A simple model-based control approach is given in chapter 7. A few future work ideas are proposed in chapter 8. The final chapter 9 concludes the work.

Chapter 2
State of the art

Electrokinetics is a research field with interest in moving with solid objects or fluid using the electric field. The theory is explained in a number of publications, I read the theory basics in [1]. For the extensive theory of electrical field and electromechanics [2] is recommended by the community. The area of interest utilizing the fluid electrokinetics the most is the liquid pumping.

Pumping of liquids through a microchannel is now a topic of interest for about three decades. This technique is used for transporting liquid through thin microchannels in one dimension (only back and forward in terms of the microchannel dimensions – its length is usually much greater than its diameter, which is in order of micrometers). The pumps themselves can be divided into two categories: mechanical and non-mechanical pumps, or in other words membrane-displacing and field induced [3].

Mechanical pumps were the first pumps developed and have been studied for over thirty-five years now. The fluid is actuated by a moving membrane and mechanical pumps achieve rates of tens of mL/min. Mechanical pumps have typically predefined volume-per-stroke capability which is unchangeable after fabrication and are also prone to mechanical damage caused by impurities in the operated liquid or material and process imperfections during fabrication. The non-mechanical pumps, which can be for example electrical as in our case, magnetical, laser based or acoustic, have the advantage in a possibility to precisely control the flow volume and velocity magnitude. Also, they are more resistant to fluid impurities and there are no moving parts which can break easily and complicate the fabrication process. Another advantage of non-mechanical micropumps is that they do not suffer from a so-called back-pressure leakage. A nice comparison of different micropumps can be seen in [4], which was the main source for this paragraph. Or alternatively, more detailed comparison is given in [5].

Concerning electrical field induced fluid motion there are two main physical phenomena causing the working fluid movement – electrothermally induced movement and electroosmotically induced movement.

2.1 Electrothermal flows

A model of electrothermal flows widely accepted by the community is published in [6] in which the authors use a low-temperature gradient assumption. This model is further extended by S. Loire in [7] who also conducted numerous experiments. However, she wanted to suppress electroosmosis in the experiments, so the voltage of up to 40 V peak to peak at a frequency of 1 MHz was chosen. Significant electrothermal fluid flow could be seen at a minimum voltage amplitude of around 15 V peak to peak. Three interdigitated linear electrodes were used and it was shown the electrothermal fluid flow is two-dimensional and perpendicular to the electrodes in this configuration. S. Loire also shows the standard model from [6] can get inaccurate at solution conductivity higher than 1 mS/m and at high voltage.

Numerical studies on electrothermal fluid flows presented in [8] and [9] both report electrothermally induced velocities with maximum values less than 10 μm/s. Potential frequencies larger than 200kHz are used in both studies, the potential amplitude ranges from 1 to 10 V. In [8] only 10 μm wide electrodes separated by the same width are considered. One order wider electrodes are considered in [9].

2.2 Electroosmosis

Concerning electroosmosis the theory is comprehensively explained by Green, Ramos, Morgan, González and Castellanos in numerous papers, i.e. in [10], [11], [12], and in their book [1]. The authors also performed various experiments using mostly interdigitated arrays of electrodes, either symmetrical or asymmetrical, reported in [12], [13] and [14]. In general, there are three ways of actuating fluid using electroosmosis – either using DC potential, AC potential (over an asymmetric electrode array) or a special kind of AC potential, a traveling potential wave (over a symmetric electrode array). The reported maximal velocity for one-dimensional pumping in a 0.2 mm high microchannel with a KCl in deionized (DI) water solution (of conductivity about 1,3 μS/m) was about 200 μm/s for traveling wave electroosmosis using an array of 20 interdigitated electrodes with 20 μm width and separated by 20 μm wide gaps. For AC electroosmosis using an asymmetric array of interdigitated electrodes of width 100 μm and 10 μm separated by 10 μm gaps the maximum pumping velocity for 20 volts peak to peak voltage at 10 kHz was about 12 μm/s.

Another theoretical text for fluid electrokinetics by J. Kirby [15] tackles electroosmosis in more extensive and more detailed fashion than in [1].

In [16] the authors present a study on AC electroosmotic pumping velocity using much smaller electrodes – up to a size of 2 μm. Their working fluid was a solution of $NaNO_3$ in DI water. For an asymmetric array with 2 μm and 10 μm long electrodes separated with 2 μm and 6 μm wide gaps the maximum pumping velocity reached almost 500 μm/s.

In [17] Lin et al. show a device for particle separation based on circular traveling wave electrosmosis. They use a circular interdigitated array of microelectrodes and 1.2 V source potential with a frequency of 2.5 kHz to separate polystyrene beads of different sizes.

As seen from above-mentioned studies, the pumping velocity is highly dependable on the electrodes geometry and spacing, the working fluid used and of course the magnitude and frequency of the applied voltage. Numerical studies on electroosmotic pumping can be seen in [12] and in [18], [19] and [20] of authors from University of Chemistry and Technology in Prague. In these publications the authors covered the relationships between the individual parameters such as solution conductivity, voltage magnitude and so on and the pumping velocity.

A comparison of experimental data is shown in Table 2.1. Please note the values in the table are not directly comparable to each other, because of the actual setups of all the experiments, i.e. the electrode material and dimensions, were different.

The concepts of traveling wave electroosmosis, AC electroosmosis, symmetrical and asymmetrical electrodes, etc. are explained in detail in the following chapter called Electroosmosis.

Paper ref.	Pump. type	Electrode geom.	El. material	El. dimensions	Solution	Voltage range	Frequency range	Max. fluid velocity
[13]	ACEO	asymmetric	Titanium/gold/ titanium sandwich	100 µm and 10 µm el. and gaps	water + KCl (1.3 mS/m)	4 - 22 V_{PP}	0.1-100 kHz	200 µm/s
[16]	ACEO	asymmetric	ITO	multiple patters, 2-25 µm sizes	water + NaNO3 (conduct. not specified)	0 - 5 V_{RMS}	1 - 3 kHz	450 µm/s
[21]	ACEO	asymmetric	10 nm NiCr and 100 nm of gold	25 µm and 4 µm el. and 4 µm and 50 µm gaps	water + NaNO3	0 - 2 V_{RMS}	0.1 - 100 kHz	120 µm/s
[13]	TWEO	symmetric	Titanium/gold/ titanium sandwich	20 µm el., 20 µm gaps	water + KCl (1.3 mS/m)	2 - 7 V_{PP}	0.1-100 kHz	12 µm/s
[17]	TWEO	symmetric circular	Titanium	5 µm el. and gaps in center	water + KCl (conduct. not specified)	1.2 V	2.5 kHz	Not specified
[22]	TWEO	symmetric circular	titanium/ aluminium	750 nm el. and gaps	water + KCl (2 - 8.4 mS/m)	0 - 1 V	10 - 2500 kHz	200 µm/s
[23]	TWEO	symmetric	10 nm titanium and 100 nm platinum	20 µm el. and gaps	water + KCl (1.5 - 16.9 mS/m)	1 - 2 V	0.1 - 10 kHz	70 µm/s
[24]	TWEO	symmetric	platinum	10 µm and 20 µm both el. and gaps	water + KCl (1.5 mS/m)	1.5 - 8 V_{PP}	0.01 - 10 kHz	300 um/s

Table 2.1. Electroosmosis experiments comparision.

Chapter 3
Electroosmosis

If an electric potential is applied to a surface in contact with a liquid, a net fluid flow above the charged surface is observed. This electrokinetic phenomenon of induced flow is called electroosmosis. The flow is generated only in the direction tangential to the charged surface. Thanks to the viscosity of the liquid the whole fluid bulk starts to move.

3.1 Electric double layer

The crucial phenomenon one has to understand while creating a model of electroosmotic flow is the formation of a so-called electric double layer (EDL). Consider a boundary between a charged surface (an electrode in our case) and an aqueous solution of an electrolyte. Ions of the opposite polarity from the electrode start to form a thin layer right next to the charged surface. Actually, the layer has two parts – Stern layer and diffuse layer.

The Stern layer (also called the compact layer or Helmholtz layer) only consists of ions of opposite polarity from the electrode which form in direct contact with the charged surface. In diffuse layer both positively and negatively charged ions appear with the prevalence of the same polarity as ions of the Stern layer – opposite to the charged electrode surface. The sketch of both layers can be seen in fig. 3.1.

In literature, the electric double layer is sometimes called induced-charge electric double layer. This term emphasizes the fact the electric double layer is created by electric field rather than chemical reactions on the interface between the charged surface and the electrolyte, which can also create a different type of double layer.

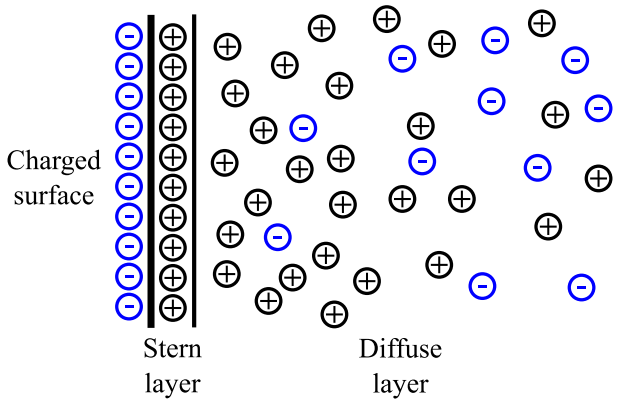

Figure 3.1. Electric double layer illustration

The interaction between the electrical double layer and an extrinsic electric field is what causes the fluid to move. The Stern layer is immovable and the fluid slip velocity is maximal at the shear plane between the Stern and diffuse layers also called the outer

Helmholtz plane. The interface between the Stern layer and the charged surface is then called the inner Helmholtz plane.

The characteristic thickness of the electric double layer is called Debye length λ_{D}, which is also sometimes defined as reciprocal Debye length κ, where $\lambda_{\mathrm{D}} = \frac{1}{\kappa}$, and it is given by

$$\kappa^2 = q^2 \sum_{i}^{n} \frac{z_i^2 n_0}{\varepsilon k_{\mathrm{B}} T}, \tag{3.1}$$

where q is ionic charge, ε is perimittivity of the fluid, n_0 is bulk concentration, k_B is Boltzmann constant, T is temperature and z_i is valence of ith (out of n total) chemical species in the solution, or alternatively

$$\lambda_{\mathrm{D}} = \sqrt{\frac{\varepsilon RT}{2F^2 I_C}}, \tag{3.2}$$

where $R = 8.3144598$ J mol^{-1} K^{-1} is the universal gas constant, T is temperature, $F = 96485.3329$s A mol^{-1} is Faraday constant and ionic strength I_C is given by $I_C = \frac{1}{2}\sum_{i=1}^{n} c_i z_i^2$, where i again refers to individual chemical species with concentration c_i and valence z_i. These relations are however only used when dealing with asymmetrical electrolytes, for symmetrical electrolytes (all the individual ion in the electrolyte have similar mobilities, for example DI water + KCl solution) the formula (3.1) simplifies to

$$\kappa^{-1} = \lambda_{\mathrm{D}} = \sqrt{\frac{\varepsilon k_{\mathrm{B}} T}{2z^2 q^2 n_0}} = K_{\mathrm{e}} \sqrt{\frac{T}{c}}, \tag{3.3}$$

where K_{e} is just a constant we get after substituting concrete values of considered electrolyte into the equation. In [19] authors also show the Debye length can be simplified as

$$\lambda_{\mathrm{D}}^2 = \frac{\varepsilon D}{\sigma}, \tag{3.4}$$

where σ is conductivity of the fluid and D is the diffusion coefficient of the fluid. The general rule is that the less conductive the solution is the larger is the value of Debye length. For highly deionized water, the Debye length is about 960 nm. For typically used electrolytes with conductivity of order of 1-10 mS/m the Debye length is less than 50 nm.

The formation of the electric double layer also depends on the frequency of the applied potential. The lowest frequency which is too high for the electric double layer to form is called a charge relaxation frequency and it is given by

$$\omega_r = \frac{\sigma}{\varepsilon}. \tag{3.5}$$

At this frequency there is simply not enough time for the ions to migrate in the fluid and form the EDL. For illustration, in table 3.1 a comparison of charge relaxation frequencies for deionized water and a KCL salt solution in deionized water is given.

Solution	Conductivity	Rel. permittivity	Charge relaxation freq.
DI water	$5.5{\cdot}10^{-6}$ S/m	80	$\approx$ 7800 rad/s $\approx$ 1240 Hz
KCl solution	$1{\cdot}10^{-3}$ S/m	80	$\approx$ 1400000 rad/s $\approx$ 223 kHz

Table 3.1. Charge relaxation frequencies comparison.

3.1.1 Debye-Hückel approximation

The concept of electrical double layer has been presented. Now we need to know how does the electrical potential applied to the wall (electrode) looks like inside the EDL and the bulk fluid. If we consider the wall curvature to be negligible, the dimension perpendicular to the wall much larger than the electrolyte Debye length λ_D, we assume a symmetrical electrolyte and we use boundary conditions $\varphi = \varphi_0$ at $y = 0$ (the wall-electrolyte interface) and $\varphi = 0$ at $y = \infty$ (in the fluid bulk), course of the local potential φ can be obtained as

$$\nabla^2\varphi = \kappa^2\varphi. \tag{3.6}$$

This approximation used is called Debye-Hückel approximation. The solution to this equation is given by

$$\varphi = \varphi_0\, e^{-\kappa y}. \tag{3.7}.$$

According to current state of theory the exponential decrease in the potential is valid only in the diffuse layer. Inside the Stern layer the potential is assumed to decrease linearly [1]. The potential through the EDL can be seen in fig. 3.2. In the figure φ_E is electric potential applied to the electrode and a so-called zeta potential ζ is potential dropped across the Stern layer. With the distance from the electrode approaching infinity in limit the potential approaches 0.

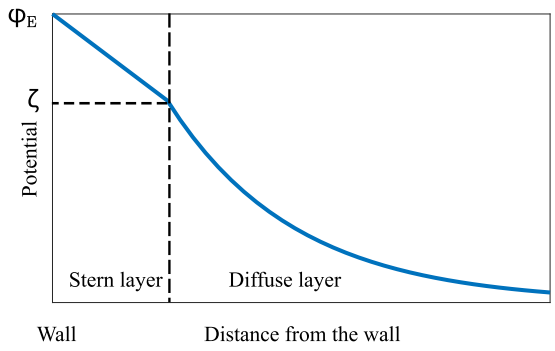

Figure 3.2. Potential inside the electrical double layer.

Evaluating the electric potential inside the double layer is not very computationally friendly if we consider domains of dimension much larger than the Debye length. Another EDL model is generally used.

3.1.2 Electric double layer as a capacitor

Charging of the double layer – the motion of ions with opposite charge to the electrode – can be modeled as charging of a capacitor. Considering two electrodes with fluid bulk between them, the model looks like in fig. 3.3, the electric double layer consists of two capacitors in series (one for Stern layer and one for diffuse layer) and the bulk electrolyte consists of a parallel connection of a capacitor and resistor.

This model is especially handy because it allows us to approximate the EDL by a boundary condition

$$\sigma\frac{\partial\varphi}{\partial y} = i\omega C_{\mathrm{DL}}(\varphi - V_{\mathrm{e}}), \tag{3.8}$$

where φ is the potential just outside the double layer, C_{DL} is the double layer capacitance and V_{e} is the potential applied to the electrode given as a phasor. This boundary

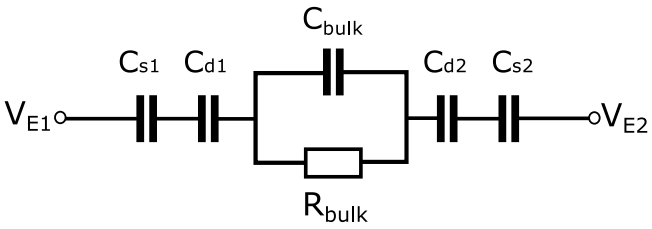

Figure 3.3. EDL modeled as a capacitor.

condition represents the charge conservation principle. The current density going inside the double layer should be the same as the current density going outside the layer.

With this boundary condition set at the electrodes and

$$\frac{\partial \varphi}{\partial y} = 0 \tag{3.9}$$

set on all other boundaries the electric potential inside the fluid bulk follows the Laplace's equation

$$\nabla^2 \varphi = 0. \tag{3.10}$$

3.1.3 Electroosmotic slip velocity

As mentioned in the beginning of this section, on the interface between charged surface and an electrolyte, the electrolyte experiences motion. Because the source of the motion is shear stress right at the interface, it can be seen as a boundary condition also called electroosmotic slip velocity. Actually, the last statement is not exact. At the very interface between the surface and the electrolyte the no slip condition as seen in any other macroscopic fluid flow still holds. The movement is generated at the outer Helmholtz plane. When considering a physical domain of characteristic size much larger than λ_D, we can neglect this difference.

The slip velocity on perfectly polarizable metal surfaces is given by the Helmholtz-Smoluchowski equation [14]

$$u = \frac{\varepsilon \Delta \varphi}{\eta} E_t, \tag{3.11}$$

where $\Delta\varphi$ is the potential drop across the double layer and E_t is electrical field tangential component to the electrode surface.

3.1.4 Further references

A detailed and easy to understand characterization of the electric double layer is provided in [25]. For more in-depth explanation, see [1] or [15] .

3.2 Fluid pumping through a microchannel

Even though our main goal was not liquid pumping through a microchannel, but more of a control of fluid and/or a microobject (immersed in the fluid) motion in a flat space of millimeter scale, the micropumps illustrate the process of actuating the liquid. Currently, there are three basic approaches to pump liquids with the electroosmosis effect. Each one of them is described in their own subsection below.

3.2.1 DC electroosmotic pumps

Pumping with application of non-alternating continuous potential was the first implemented electroosmotic principle [4]. The principle of DC electroosmotic pumping is as follows. We consider a microchannel with some charge at the walls, which most materials have even in small amounts, then at the interface between the microchannel wall and the working fluid electrical double layer forms. After applying electrical field along the longest dimension of the microchannel, the fluid at the interface between the microchannel and the fluid starts to move and as a consequence the whole fluid bulk starts to move in the same direction. The principle is illustrated in fig. 3.4

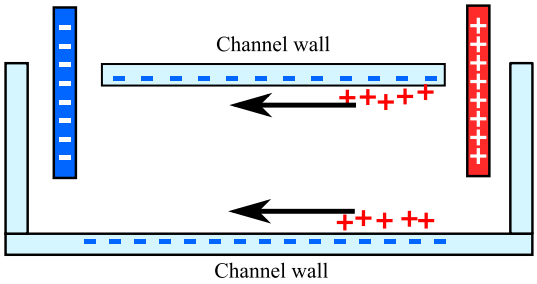

Figure 3.4. DC Electroosmosis principle.

The slip velocity at the wall-fluid interface is given by the already introduced Helmholtz-Smoluchowski equation (3.11).

This pumping would seem quite easy to do, however as reported in the literature [26], [3], [5] the electrical potential applied to the electrodes has to be in order of kilovolts. This is the reason I did not consider DC electroosmosis as a good candidate for my experiments shown further in the thesis.

3.2.2 AC electroosmotic pumps

Another option for fluid pumping in a microchannel is AC electroosmotic pumping. Now a different electrode geometry and arrangement has to be used. It is called an interdigitated electrodes array and for AC electroosmosis, there are 3 viable options as shown in fig. 3.5.

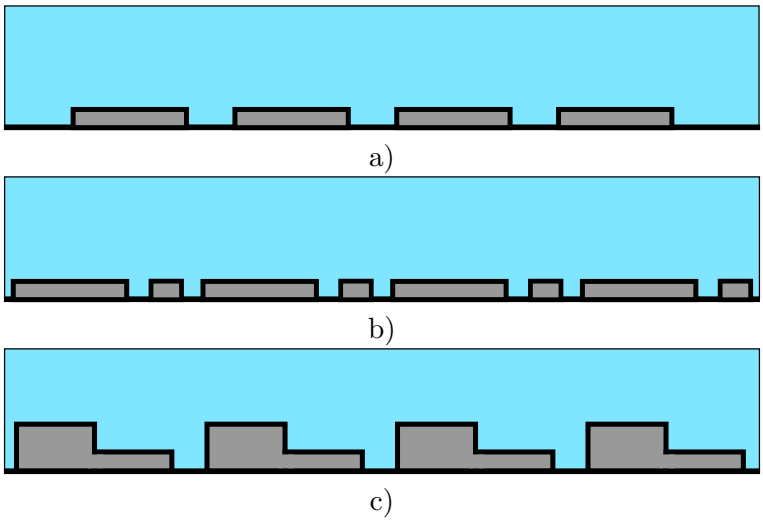

Figure 3.5. Three possible interdigitated electrode array layouts.

For the first geometry (fig. 3.5 a)), all the electrodes have the same width and all the gaps between them are also equal. Over every odd electrode an AC potential is applied and over every even electrode the same potential phase shifted by 180° is applied. However for this geometry, the time averaged velocity in the horizontal direction is zero. The only visible movement can be seen in fig. 3.6 b). In fig. 3.6 a), the direction of the induced electroomotic slip velocity (which is the same as the direction of force $\mathbf{F}_q$) in comparison with the tangential electric field is given.

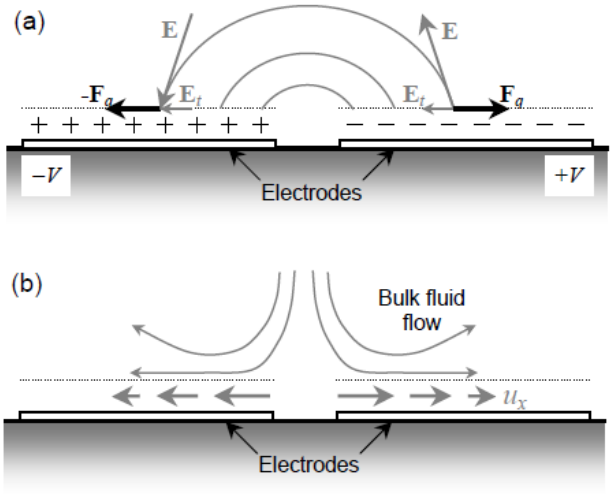

Figure 3.6. AC Electroosmosis principle. The image is taken from [1].

The magnitude of time averaged AC electroosmotic slip velocity is given by [1] and [12] as

$$\langle u_x \rangle = \frac{1}{8} \frac{\varepsilon \varphi_0^2 \Omega^2}{\eta x (1+\Omega^2)^2}, \tag{3.12}$$

where Ω is the non-dimensional frequency

$$\Omega = \frac{1}{2} \frac{\pi \kappa x \varepsilon \omega}{\sigma}, \tag{3.13}$$

x is the horizontal coordinate and ω is the angular frequency of the applied AC electrical potential. What might cause some kind of confusion is the x coordinate in the formulas. It represents the distance from the center of the gap between the electrodes. The formula (3.12) is an analytical solution of the Helmholtz-Smoluchowski equation (3.11) for the case of the parallel electrodes.

However one has to bear in mind significant simplifications were done when deriving (3.11). The largest one is ignoring the slip velocity generated at the outer edges of electrodes. The slip velocity there is considered neglectable. To illustrate, a visualisation of the electric field lines is presented in fig. 3.7 (lines of $\mathbf{E}$ are displayed in orange, the direction vectors are displayed in blue and the two electrodes are black), the equation (3.11) neglects the effects of electric field $\mathbf{E}$ (right above the electrodes) wherever its tangential direction is not the direction to the center of the electrodes for the left negatively charged electrode and wherever its tangential direction actually is the direction to the center of the electrodes for the left negatively charged electrode. The direction of the electric field also gives the direction of the fluid flow.

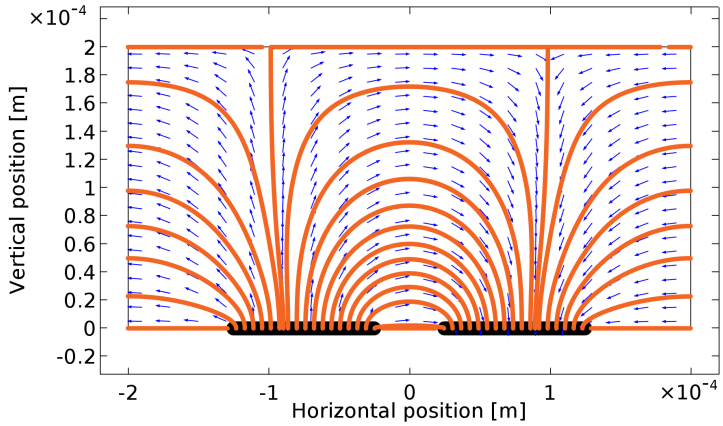

Figure 3.7. Electric field **E** visualisation for two parallel electrodes. The left one is positively charge, the right one is negative.

Experimentally the neglected slip velocity can be seen as small rolls of fluid created at the outer edges of the electrode. An expression which takes all the surface area to consideration is then given by [11] and [19] as

$$\langle u_x \rangle = -\frac{\varepsilon}{4\eta}\Lambda\frac{\partial}{\partial x}(\varphi - V_j)(\varphi - V_j)^*, \tag{3.14}$$

where φ is electric potential right outside the double layer, η is viscosity of the fluid and Λ is a ratio between Stern layer capacitance and diffuse layer capacitance, V_j is the potential applied to the (jth) electrode, and $*$ superscript expresses a complex conjugate, or also alternatively [14]

$$\langle u_x \rangle = -\frac{\varepsilon}{2\eta}\mathrm{Re}\left[\Delta\varphi\frac{\partial\varphi^*}{\partial x}\right] = \Lambda\frac{\varepsilon}{2\eta}\mathrm{Re}\left[\frac{i\sigma}{\omega C_{\mathrm{DL}}}\frac{\partial\varphi}{\partial y}\frac{\partial\varphi^*}{\partial x}\right], \tag{3.15}$$

where $\Delta\varphi$ is the potential drop across the double layer and i is a complex imaginary unit. Again the slip velocity u_x is time averaged. Both equations are valid and are just different expressions for the same.

The same discussion about the formulas also holds for the second electrode array geometry displayed in fig 3.5 b). Again the electrodes potentials are the same as above. Since the electrodes are not symmetric in width (which is also the reason this geometry is in literature called asymmetric electrode array) the time averaged horizontal fluid velocity generated is not zero and the sketch of this principle is shown in fig. 3.8 a). This design is however harder to fabricate because the small electrode rises the needs for fabrication details.

The remaining electrode array design shown in fig 3.5 c) could also generate non-zero horizontal flow velocity and is even harder to fabricate than the last presented design because it requires a 3D structure to be made. The principle of pumping is again the same, but the novel idea is to hide the small whirls of fluid in the array as shown in fig. 3.8 b). For more details see a theoretical prediction paper by Bazant and Ben [27].

3.2.3 Traveling wave electroosmotic pumps

We would like to benefit from the fact the symmetrical planar interdigitated electrode arrays are the easiest to fabricate out of all three types presented above. And to make the time averaged slip flow velocity non-zero a new concept of applying the electrical potential has to be introduced. It is called the traveling wave potential. What it means

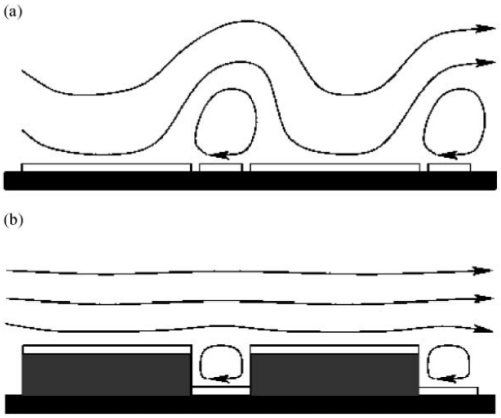

Figure 3.8. AC Electroosmosis (a) asymmetrical and (b) 3D electrode array design principles. Also called fluid conveyor belt. The image is reprinted from [27].

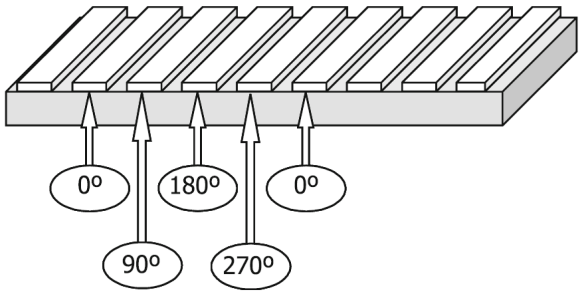

Figure 3.9. Traveling wave electroosmosis electrode potentials. The image is reprinted from [28].

is we apply AC potential at the electrodes, but each two neighbouring electrodes have the potential phase shifted by 90° as displayed in fig. 3.9.

3.3 Other electrokinetic phenomena

Apart from electroosmosis, other physical phenomenons also occur when the electric field interacts with liquid and floating particles and micro objects.

3.3.1 Electrothermally induced fluid flow

A fluid motion observable for a large spread of frequencies is an electrothermally induced fluid flow. For this kind of flow a conductive working fluid is considered. When applying an electric potential to a conductive fluid, an electrical current passes through it generating heat. Because the field is non-uniform, the heat generation is also non-uniform and the diffusion of heat through the system is rapid, leading to a static thermal field. Variations in the temperature field lead to variations in the local conductivity and permittivity of the fluid. These gradients in conductivity and permittivity then impose an electrical force on the fluid [8].

By way of illustration, the total power generated per unit volume is given by

$$W = \sigma E^2. \tag{3.16}$$

For an electrolyte with conductivity of $\sigma = 0.01\text{S m}^{-1}$ and an electrical field of $4 \cdot 10^5$ V m^{-1} (corresponding to an applied voltage of 10 V in a gap of 25 μm), W equals to $1.6 \cdot 10^9$ W m^{-3}. Since we are interested in system of a micro scale, the power dissipation in such amount of space will be in order of tens of mW [6].

Electrical forces $\mathbf{F_E}$ in the fluid are given by [28]

$$\mathbf{F_E} = \rho_\mathbf{q}\mathbf{E} - \frac{\mathbf{1}}{\mathbf{2}}|\mathbf{E}|^2\nabla\varepsilon + \frac{\mathbf{1}}{\mathbf{2}}\left(\rho_\mathbf{m}\left(\frac{\partial\varepsilon}{\partial\rho_\mathbf{m}}\right)|\mathbf{E}|^\mathbf{2}\right), \tag{3.17}$$

where ρ_q is free electrical charge density and ρ_m is mass density.

In this thesis however the electrothermal induced fluid flow is not further used nor studied. It is simply because the experiments conducted in [7] and [6] differed in the parameters from the area we are interested in with electroosmosis. The voltage used was higher (more than 25 V peak to peak) and even with this voltage the fluid velocity was significantly lower (less than 10 μm/s) than velocity we are expecting (> 100 μm/s). And mostly, the fluid used were two orders more conductive than deionized water which was the main pumping fluid used in this thesis.

Nonetheless it is important to take into consideration the possibility of electrothermal fluid pumping. It can disturb experiments with other parameters than those considered in further chapters.

3.3.2 Dielectrophoresis

Every charged particle experiences motion in a uniform electric field. The force acting on such particle is called electrophoretic. Negatively charged particles move to positively charged source and vice versa for positively charged particles. In this thesis only AC source potential is considered. Since the electrophoretic effect of such potential is oscilatory with zero mean, we safely neglect the electrophoretic forces.

However when applying AC potential over a medium in which there are electroneutral particles immersed with significantly different electrical properties (particularly permittivity and conductivity) than the medium a so-called dielectrophoretic force is then observable. The non-uniform electric field induces a dipole inside the particle, which is essential for giving rise to the dielectrophoretical force.

The dielectrophoretical force $\mathbf{F}_\text{DEP}$ (also called conventional dielectrophoretic force) acting on a particle is proportional to the gradient of squared electrical field, namely

$$\mathbf{F}_\text{DEP} = \pi\varepsilon_\text{m} r^3 \text{Re}\left[\frac{\varepsilon_\text{p}^* - \varepsilon_\text{m}^*}{\varepsilon_\text{p}^* + 2\varepsilon_\text{m}^*}\right]\nabla\mathbf{E^2}, \tag{3.18}$$

where r is radius of the particle, ε_m is permittivity of the medium and ε_p is permittivity of the particle, the $*$ subscript indicates we are talking about complex perimittivity defined as $\varepsilon^* = \varepsilon\varepsilon_0 - i\frac{\sigma}{\omega}$, where i is complex unit and ε_0 is permittivity of free space.

When dealing with a traveling wave potential the dielectrophoretic force has a new component

$$\mathbf{F}_\text{DEPtw} = \pi\varepsilon_\text{m}\text{r}^3\text{Im}\left[\frac{\varepsilon_\text{p}^* - \varepsilon_\text{m}^*}{\varepsilon_\text{p}^* + 2\varepsilon_\text{m}^*}\right](\text{E}_\text{x}^2\nabla\varphi_\text{x} + \text{E}_\text{y}^2\nabla\varphi_\text{y} + \text{E}_\text{z}^2\nabla\varphi_\text{z}). \tag{3.19}$$

The resulting dielectrophoretic force is then a sum of the two forces (3.18) and (3.19). The fraction

$$K(\omega) = \frac{\varepsilon_\text{p}^* - \varepsilon_\text{m}^*}{\varepsilon_\text{p}^* + 2\varepsilon_\text{m}^*}, \tag{3.20}$$

taking part in both equations is called Clausius–Mossotti relation or factor.

We distinguish two types of dielectrophoresis – positive and negative. In positive dielectrophoresis ($\mathrm{Re}[K(\omega)] > 0$) the particle experiences pull to a position with higher field strength (towards the electrode edges) and in negative dielectrophoresis ($\mathrm{Re}[K(\omega)] < 0$) the particle moves towards a position with lower electric field strength (away from the electrode edges) [28].

Now one can ask why do we talk about dielectrophoresis in this text when we consider liquid flow control. In a homogeneous liquid no dielectrophoretic force affects the movement of the liquid molecules. As it will be explained in further chapters to measure the liquid velocity small particles dispersed in the liquid are used. Then one has to be aware of a possible dielectrophoretic force acting on the particle. To minimize the dielectroosmosis force the immersed particles should be as small as possible since the force is proportional to a cube of the particle radius.

More on dielectrophoresis can be found in multiple theses written at Czech Technical University, which were also the source for this section [29], [30], [31].

3.3.3 Brownian motion

A phenomenon not connected to the electrical field, but also important to have in mind, is Brownian motion. It describes a random motion of particles suspended in a fluid due to collisions with atoms and molecules of the fluid itself. This motion can be modeled as a stochastic random walk. A root-mean-square displacement in one direction x is given by [32]

$$\Delta x = \sqrt{\frac{k_\mathrm{B} T}{3\pi r \eta} t_\mathrm{O}}, \tag{3.21}$$

where t_O is an observation period of time. Always, we have to bear in mind the forces we would like to move the particles with should have greater effect on theirs motion than Brownian motion. In this thesis, we expect to move the fluid and the particles at velocities much greater than 1 µm/s and therefore Brownian motion should not bother us. We should, however, be aware of its disturbative effects when dealing with very small particles (< 1µm diameter).

Chapter 4
Mathematical model

Electroosmotic phenomenon explained in the last chapter was mathematically modelled and simulated in a commercial finite element method (FEM) solver COMSOL Multiphysics v5.1. It allows users to create their own geometries in one, two and three space dimensions and then introduces either user-defined or predefined partial differential equations (PDEs) to be solved over these created geometries.

4.1 Briefly on finite element method

A finite element method solution to a given problem is in general obtained after 5 steps. The whole process is illustrated on an example of mechanical deformation of a microchip caused by Ohmic heat in fig. 4.1.

1. First of all, we need to define the geometry of our domain – a physical space in which we are interested in knowing a magnitude/direction/etc. of a desired quantity.
2. We define the PDEs of our problem. Usually, the a weak formulation of the PDEs has to be determined.
3. The geometry defined earlier has to be split to a so-called mesh. A set of simple geometrical elements of the same space dimension as the dimension of our problem domain. It is very important to choose an appropriate mesh, since choosing too sparse (even too dense in some cases) mesh can lead to getting totally wrong results.
4. Solving the problem PDEs using discretization in space and time and time-stepping.
5. The solution is already known. Now it is important to visualise the solution in a way a human can understand it or to post-process the results before analysing them in another script or computer program.

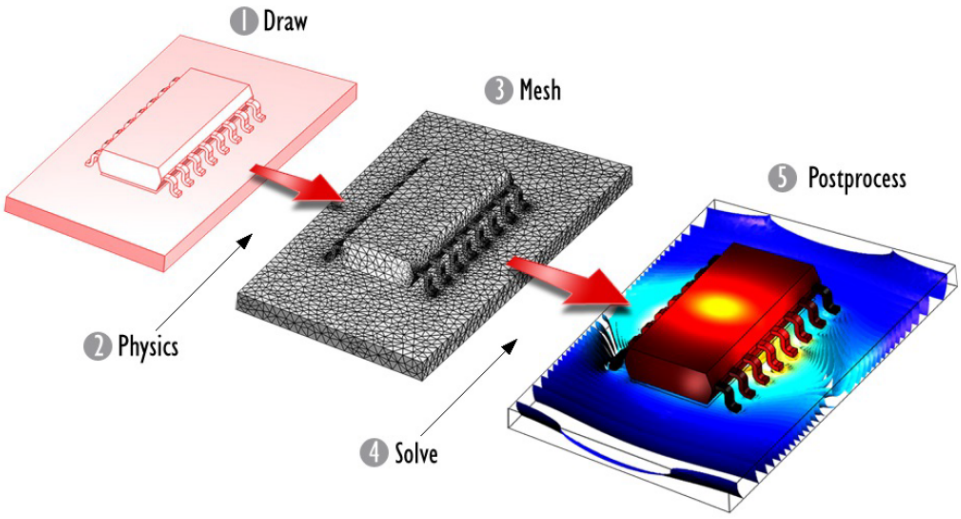

Figure 4.1. An illustration of problem solving using FEM. The image is taken from [33].

4.2 Governing equations

In all of the electroosmosis models created, electrical field and fluid dynamics have to be simulated. For both of those a physical interface is already predefined in COMSOL. The electrical field is included under the Electrostatics physics interface, which simulates Gauss's law (also one of the four Maxwell's equations)

$$\nabla \cdot \mathbf{D} = \rho_E, \tag{4.1}$$

where $\mathbf{D}$ is an electric displacement field, also given by $\mathbf{D} = \varepsilon_0 \mathbf{E}$ with ε_0 representing the dielectric constant for free space, and ρ_E is the electric charge density. And for the electric potential we have

$$\mathbf{E} = -\nabla \varphi. \tag{4.2}$$

However, for simplier modelling of the electric double layer approximation (as described for example in [11], [14] and [19]), namely the boundary conditions, the electrical field was modelled using Coefficient form PDE COMSOL physics interface.

For simulating the fluid dynamics the COMSOL interface Creeping flow is used. Creeping flow (also called Stokes flow) resembles fluid flow at low Reynolds number ($Re < 1$) given by

$$Re = \frac{\rho U L}{\eta}, \tag{4.3}$$

where ρ is the fluid density, U is the characteristic fluid velocity, L is the characteristic length of the system and η is dynamic viscosity. For our case we assume $\rho = 1000\text{kg m}^{-3}$, $U = 1 \cdot 10^{-3}\text{m s}^{-1}$, $L = 100$ µm and $\eta = 1.002 \cdot 10^{-3}\text{Pa s}$, then $Re = 0.1$. The Reynolds number represents the ratio between inertial and viscous forces in the fluid. In our case, the viscous forces dominate. For low Reynolds number (less than approximately 2000) the flow in the fluid is laminar (or creeping for even lower Reynolds number), for high Reynolds numbers the flow is turbulent.

The main equation for general fluid flow simulation is Navier-Stokes equation

$$\rho(\frac{\partial \mathbf{u}}{\partial t} + \mathbf{u} \cdot \mathbf{u}) = -\nabla p + \nabla \cdot (\eta(\nabla \mathbf{u} + (\nabla \mathbf{u})^T)) - \frac{2}{3}\eta(\nabla \cdot \mathbf{u})\mathbf{I} + \mathbf{f}, \tag{4.4}$$

where $\mathbf{u}$ is the fluid velocity, p is pressure, $\mathbf{I}$ is identity matrix and $\mathbf{f}$ are external forces applied to the fluid. The first term $\rho(\frac{\partial \mathbf{u}}{\partial t} + \mathbf{u} \cdot \mathbf{u})$ represents the time change and the inertial forces in the fluid, the second term $-\nabla p$ represents pressure forces and the third term $\nabla \cdot (\eta(\nabla \mathbf{u} + (\nabla \mathbf{u})^T)) - \frac{2}{3}\eta(\nabla \cdot \mathbf{u})\mathbf{I}$ stands for viscous forces. Since the Reynolds number is low, the inertial term can be neglected – this is actually the difference between creeping flow and laminar flow, in laminar flow, the inertial term is not neglected. Also, the time-dependant term is neglected, because we are interested only in the steady state. When dealing with incompressible liquids the term $-\frac{2}{3}\eta(\nabla \cdot \mathbf{u})\mathbf{I}$ is also neglected. With these mentioned assumptions (low Re, incompressible liquid) Navier-Stokes equation is simplified to Stokes equation

$$\eta \nabla^2 \mathbf{u} - \nabla p + \mathbf{f} = 0. \tag{4.5}$$

The (Navier-)Stokes equation is solved in Creeping flow interface together with continuity equation

$$\frac{\partial \rho}{\partial t} + \nabla \cdot (\rho \mathbf{u}) = 0. \tag{4.6}$$

We assume all the fluids to be incompressible, so the continuity equation (4.6) simplifies to

$$\nabla \cdot \mathbf{u} = 0. \tag{4.7}$$

4.3 Boundary conditions

All the presented governing equations in the previous section are solved inside a bounded space. On a boundary, various boundary conditions are implemented. For the electric problem, the boundary conditions differ for various models and they are going to be given separately for individuals models considered further.

For hydrodynamics problem the boundary conditions are similar for all the created models. On the boundary between an electrode and the fluid bulk a slip velocity boundary condition is considered. Over all the other boundaries corresponding to glass or PDMS (a silicon based polymer forming walls and introduced in further chapters) and fluid bulk transitions are no-slip velocity boundary conditions. When there is no glass or PDMS wall either open boundary or periodic boundary conditions are used. These boundary conditions are specified for individual models.

The numerical simulation of hydrodynamic problem in COMSOL also requires users to specify a pressure point constraint with a selected arbitrary value anywhere inside the computational domain.

4.4 Two electrode AC electroosmosis model

To understand basics of AC electroomotic phenomenon, a simple two electrode model was created. The geometry of the model can be seen in fig. 4.2. We assume the electrodes to be infinitely long, so we are going to simulate only a 2D slice. Also we assume the electrodes to be infinitesimally thin, which is reasonable, because the height of the electrodes is usually in order of tens to hundreds of nanometers. These two assumptions are used in all 2D models in this thesis.

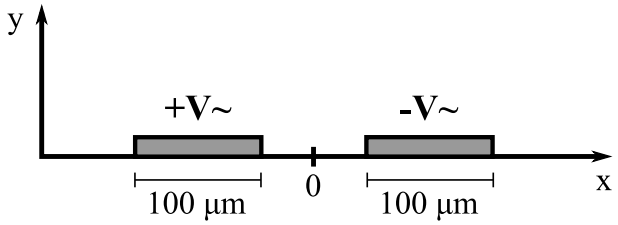

Figure 4.2. Two electrode AC electroosmosis model geometry

The simplified time averaged electroosmotic slip velocity at the electrodes is given by eq. (3.12), which is

$$\langle u_x \rangle = \frac{1}{8} \frac{\varepsilon \varphi_0^2 \Omega^2}{\eta x (1+\Omega^2)^2},$$

where

$$\Omega = \frac{1}{2}\frac{\pi\kappa x\varepsilon\omega}{\sigma}.$$

A parametric study of this equation applied to two imaginary electrodes with infinitesimally small gap between them is given in fig. 4.4. When it is not said otherwise, the parameters are set as deionized water is assumed to be the working fluid. The specific values can be seen in table 4.1. The potential amplitude and frequency stated in table 4.1 are arbitrary values used only for this parametric study. Also, please note that if changing the value of fluid conductivity σ or diffusivity D, Debye length has to be recalculated according to eq. (3.4).

Parameter	Symbol	Value	Unit
Diffusivity	D	$2 \cdot 10^{-9}$	$m^2\ s^{-1}$
Potential amplitude	V	5	V
Potential frequency	f	100	Hz
Relative permittivity	ε	80	-
Debye length	λ_D	900	nm
Dynamic viscosity	η	$1.002 \cdot 10^{-3}$	Pa s

Table 4.1. Typical parameter values for highly deionized water.

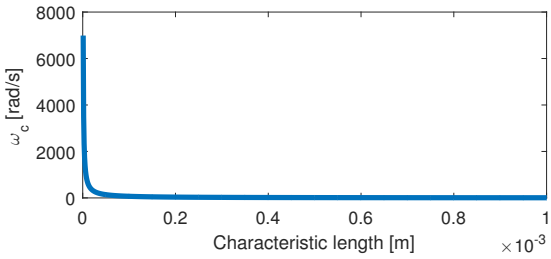

Figure 4.3. Dependency of ω_c on characteristic length of the system L

As we can see from fig. 4.4, we would like to minimize the gap between the electrodes to achieve the highest magnitude of the slip velocity. The potential angular frequency for which the slip velocity should be the greatest (assuming only frequency is changing) is given by

$$\omega_c = \frac{\sigma\lambda_D}{\epsilon L},$$

where L is characteristic length of the system. The larger this length the lower the frequency required. The relation between ω_c and L can be seen in fig. 4.3. With geometries of size more than 20 µm, ω_c is less than 350 rad s^{-1}, which corresponds to frequency of approximately 50 Hz.

In fig. 4.4 c) we observe the slip velocity gets larger when the fluid conductivity gets lower. If we increase the fluid conductivity σ, to achieve similar slip velocities as with less conductive fluid we would have to also increase the potential frequency. We could also increase potential amplitude, however the increase needed might not be possible or would cause undesirable chemical side effects.

Another approach for maximizing the slip velocity with respect to angular frequency of the applied potential is to let the dimensionless frequency Ω approach value of 1 by changing the potential frequency.

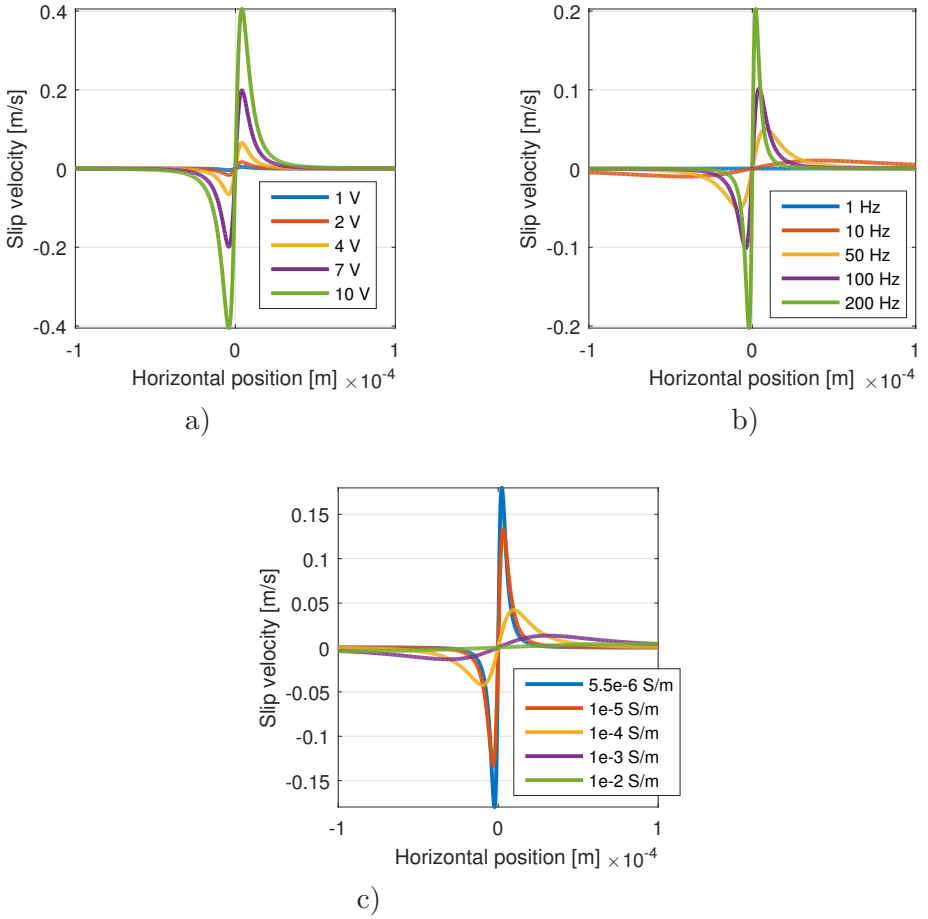

Figure 4.4. Individual parameter influences on generated slip velocity - (a) change of potential amplitude, (b) change in potential frequency and (c) change of conductivity of the fluid.

Now to extend the slip velocity to the whole fluid bulk, Navier-Stokes equation (4.4) was simulated in COMSOL Multiphysics. In this case, the electrical field does not have to be estimated. The Creeping flow interface is set up as follows, equations (4.4) and (4.7) are solved in the fluid bulk (DI water in this case) and on almost all of the boundaries a no-slip condition is applied, only on the fluid-electrode boundaries the slip condition with velocity given by equation (3.12) is used.

The resulting velocity field can be seen in figure 4.5. Both the electrodes are located on the lower boundary of the domain with y coordinate equal to 0. The left electrode is ranging from -125 µm to -25 µm and the second one from 25 µm to 125 µm, the gap between the electrodes is 50 µm wide. Note the arrows are logarithmically proportional to the corresponding fluid velocity. The magnitude of the velocity is shown as a color surface plot. As shown earlier, for AC-electroosmosis the applied potential creates opposite slip velocities on both electrodes with the highest values closest to the gap between the electrodes.

The two rolls shown in fig. 4.5 have roughly the same shape as experimental mesurements shown in literature, i.e. in [1].

There is also the second approach for computing the electroosmotic slip velocity, which does not neglect the outer edge slip velocity magnitude. We will use the equation (3.14)

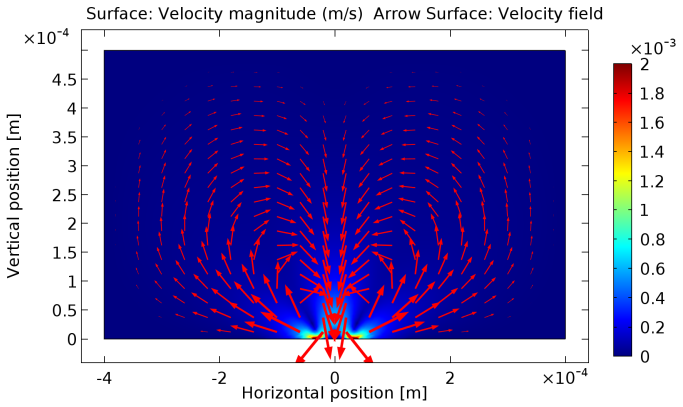

Figure 4.5. Two electrode AC electroosmosis generated velocity field using eq. (3.12).

$$\langle u_x \rangle = -\frac{\varepsilon}{4\eta}\Lambda\frac{\partial}{\partial x}(\varphi - Vj)(\varphi - Vj)^*,$$

which will especially come as handy when dealing with multiple phases of the applied potential later. To use this equation, we need to compute the electric field in the bulk close to the electrodes. To do so, we will compute the Laplace equation (4.2). To approximate the effect of the electrical double layer as explained in previous chapter the (3.8) boundary condition has to be used

$$\sigma\frac{\partial\varphi}{\partial y} = i\omega C_{\mathrm{DL}}(\varphi - V_j),$$

where V_j is the electrical potential given as a phasor applied to the jth electrode and C_{DL} is the capacitance of the electrical double layer given by

$$C_{\mathrm{DL}} = \frac{\varepsilon}{\lambda_D}.$$

In COMSOL Multiphysics, the Laplace equation with this boundary condition cannot be anymore easily simulated using the Electrostatics interface. It is necessary to use a weak form boundary condition, which I did not manage to adjust appropriately. Instead a Coefficient form PDE interface for solving custom partial differential equations was used. In Coefficient form PDE interface a PDE in form of

$$e_a\frac{\partial^2 X}{t^2} + d_a\frac{\partial X}{\partial t} + \nabla\cdot(-c\nabla X - \alpha X + \gamma) + \beta\cdot\nabla X + aX = f, \tag{4.8}$$

where X is the dependant variable (which corresponds to φ in our case), t is time, a, e_a and d_e are arbitrary coefficients, c is a diffusion coefficient, α and β are vector convection coefficients, γ is a vector flux source and f is a source term. We set all the coefficients to zero, except for c, which we set to one. Now the Coefficient form PDE has a form of Laplace equation

$$\nabla^2\varphi = 0.$$

The boundary condition (3.8) is than added as a Flux/Source boundary condition interface in COMSOL. The base form of the boundary condition is

$$-\mathbf{n}\cdot(-c\nabla X - \alpha X + \gamma) = g - qX, \tag{4.9}$$

where we set the terms $g = V_j(\frac{i\omega C_{\mathrm{DL}}}{\sigma})$ and $q = \frac{i\omega C_{\mathrm{DL}}}{\sigma}$, $\mathbf{n}$ is a normal vector of the boundary, c, α and γ are already known from (4.8). The electrical potential at the electrodes now has to be defined as complex potential – a phasor.

It is now possible to numerically compute the potential drop across the double layer. We have also done so and the result is given in fig. 4.6 – only the potential over the lower boundary is displayed.

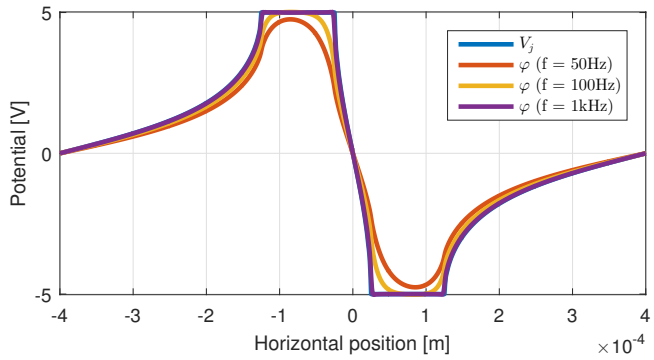

Figure 4.6. Potentials over the electrodes (the flat regions).

As we can see the larger the frequency is, the lower the potential drop (the difference between potential applied to the jth electrode V_j and potential right above the EDL φ). For $f = 1\mathrm{kHz}$ there is no potential drop - the purple and blue curves match exactly. This relation has a simple explanation. With higher frequencies there is less time for ions to form the actual double layer and so there is less potential dropped. A frequency where no potential is dropped over the double layer has already been introduced in previous chapter, its name is charge relaxation frequency and it is given by eq. (3.5).

Now we have the electric field problem sorted out, the boundary slip velocity condition for the Navier-Stokes equation can be replaced with equation (3.14). With this second approach almost the same shape of the velocity field as shown in fig 4.5 can be seen. The new result is shown in fig. 4.7. If we compare fig. 4.5 and fig. 4.7 closer. We can see small rolls of fluid at the outer edge of the electrodes. For clearer look at the expected fluid velocity field, fig. 4.8 is also included.

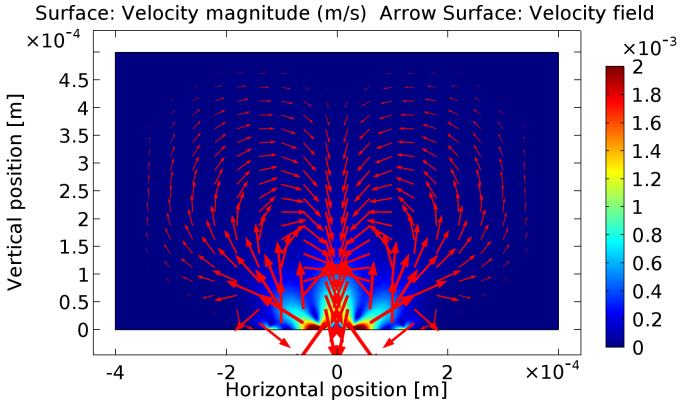

Figure 4.7. Two electrode AC electroosmosis velocity field generated using formula (3.14).

A comparison of fluid velocity magnitudes at two different height is presented in fig. 4.9. In this figure both modelling approaches are compared. Shape of the green curve in fig. 4.9 a) – the slip velocity – is the same as reported in [34].

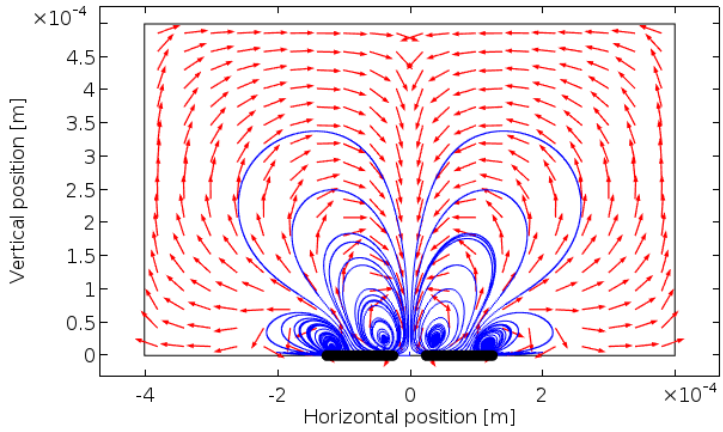

Figure 4.8. Another look at two electrode AC electroosmosis velocity field generated using formula (3.14). The red arrows lengths are normalized regardless of the actual velocity field values at individual points.

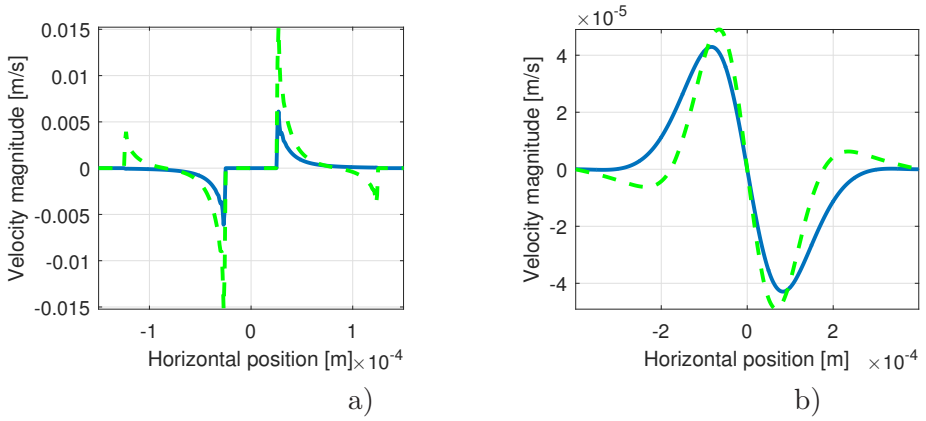

Figure 4.9. Fluid horizontal velocities at height (a) 0 (at boundary) and (b) at height 200 µm above the electrodes. Blue curves are for formula (3.12), green for (3.14).

As we can see, the two approaches yield different results. This is a result of a lot of uncertainties in various parameters which then enter each model in a different way. For example the Debye length λ_D is only a trained estimate, also the ratio Λ between the capacitance of Stern layer and the capacitance of diffuse layer is an estimate, the correct values are not yet even known to the electrokinetics community.

Eq. (3.12) is a simplified version of (3.14), the advantage is in the computational needs, since it does not need the electrical field estimated. However it comes at a cost of only approximated results.

Now if we introduce more parallel electrodes, we cannot achieve to set the liquid to move in another fashion than the whirls displayed in fig. 4.5. We can see it in fig. 4.10. By adding more electrodes we multiply the number of the whirls. To actuate the liquid in a way we could later take control of – to achieve non-zero net flow in horizontal axis – some kind of asymmetry has to be introduced.

4.5 Asymmetric electrode array AC electroosmosis

As both the model and experiments suggest simple varying the voltage amplitude or frequency over a particular subset of electrodes is not enough to achieve non-zero horizontal net flow. One of the successful approaches (as mentioned already in chapter

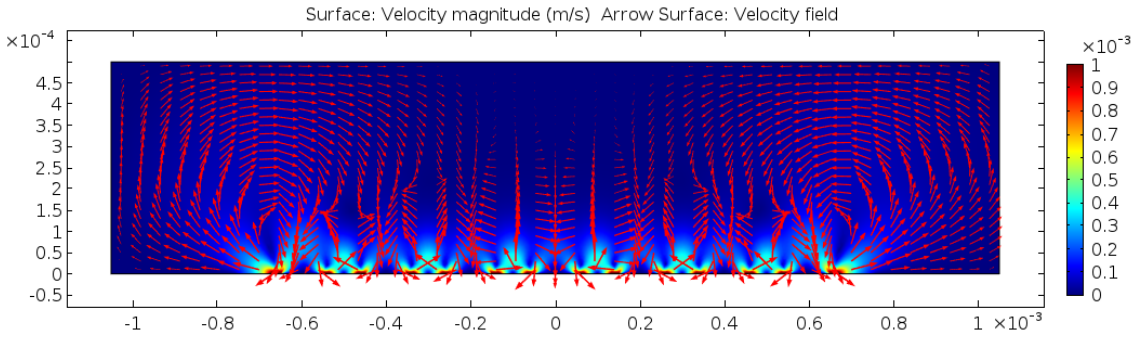

Figure 4.10. AC electroosmosis velocity field generated by 8 parallel symmetric electrodes.

3) is however to introduce asymmetry to the electrodes themselves as described in e.g. [13] or [16]. By making one of the electrodes smaller than the other the whirls over the electrodes also become asymmetrical and create the desired one directional net fluid flow.

The equations used for computing the slip velocity remain still the same – eq. (3.12) for the simplified version and eq. (3.14) for more precise numerical study.

To really see the net fluid flow velocity, the left and right boundaries are made periodic. One might ask what would introduction of periodic flow boundaries make with the velocity flow shown earlier in fig. 4.5 or fig. 4.10 and the answer is nothing. The fluid flow field would stay the same shape. We can see the velocity field on the left a right edges of our computational domain is tangential to the wall boundary surface.

The velocity field after introducing asymmetry to the electrodes can be seen in fig. 4.11. The electrodes are shown in black. The velocity field magnitude surface color plot is now omited, since it is very similar to the ones already presented. The magnitude of the velocity is by far the greatest at the electrode surfaces and it is the greater the lower is the distance between a particular position and the center of the electrodes.

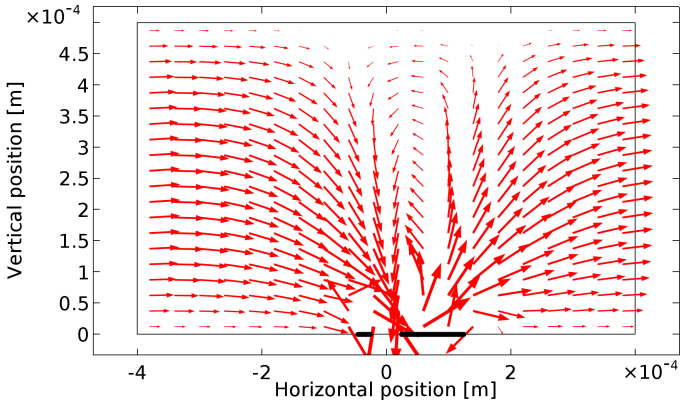

Figure 4.11. AC electroosmosis velocity field generated by 2 asymmetric electrodes.

To give an idea of how large the horizontal velocity magnitude is in the bulk liquid. The slice of the velocity field at two different y positions is show in fig. 4.12. The parameters used to get this velocity are DI water and sinusoidal voltage of 5 V amplitude with frequencies of 50 and 100 Hz.

To move the liquid over larger dimension we can put multiple electrode pairs one next to each other. The resulting geometry and the velocity field generated for asymmetric electrode array with electrodes of widths 20 μm and 100 μm with the gap between the

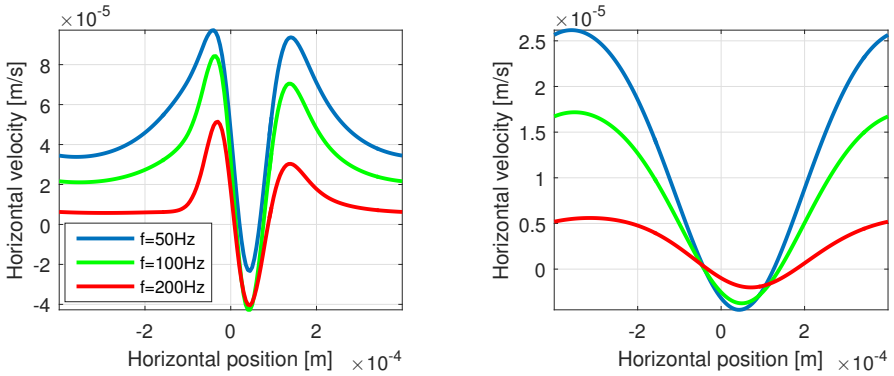

Figure 4.12. The horizontal velocity for two asymmetric electrode AC electroosmosis at (a) 100 µm and (b) 400 µm above the electrodes.

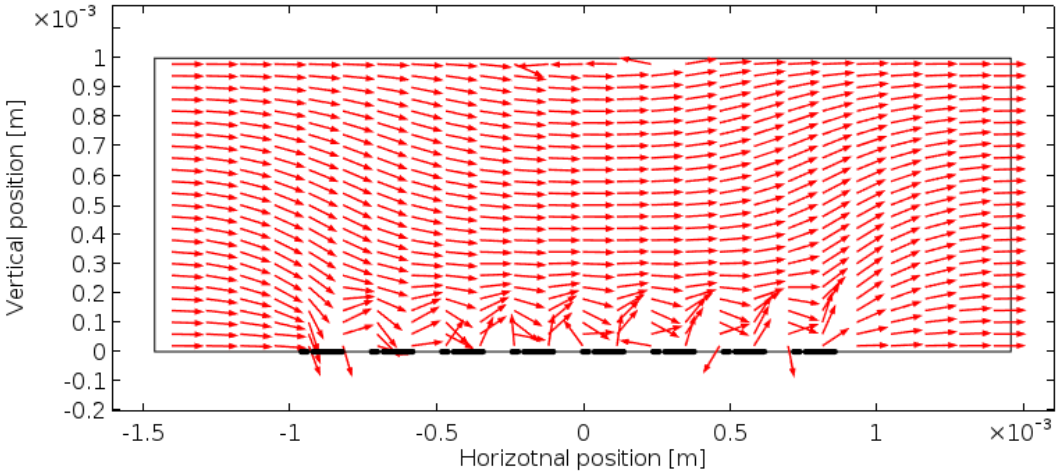

Figure 4.13. AC electroosmosis velocity field generated by 8 asymmetric electrode pairs.

electrodes 20 µm and the gap between two electrode pairs 100 µm is presented in fig. 4.13.

4.6 3D electrode design

Out of curiosity also a 3D electrode design was done in COMSOL. The resulting velocity field can be seen in fig. 4.14. In the study there are four electrodes with width of 100 µm with a step of 10 µm in the middle – the electrode has two equally wide parts, one 50 µm wide elevated by 10 µm and one on the lower wall. The geometry was chosen so it might be possible to fabricate this design in the future.

The velocity field is more turbulent and the net flow velocity generated is for 5V and 100Hz potential about 10 µm/s.

Because no such 3D electrode design was fabricated during work on this thesis, it will not developed any further.

4.7 Travelling wave electroosmosis

For the model of travelling wave electroosmosis, the same modeling approach has been used with the same equations as states in previous electroosmosis models.

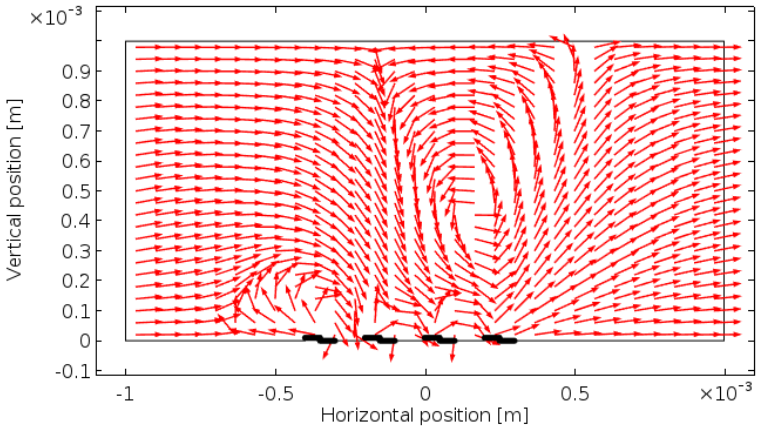

Figure 4.14. AC electroosmosis velocity field generated by 3D asymmetric electrode pairs.

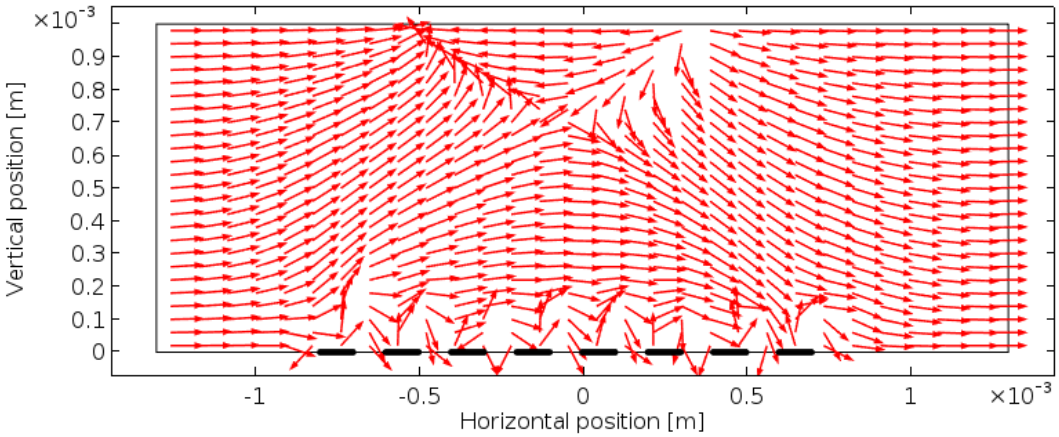

Figure 4.15. Travelling wave electroosmosis velocity field generated by 8 symmetric electrodes.

The resulting velocity field for 4-phase travelling wave is show in fig. 4.15. Again 100Hz voltage with 5V amplitude was used. The net fluid flow at 200 µm above the electrodes is about 50 µm/s.

4.8 The effect of dielectrophoresis

As stated in the previous theoretical section a dielectrophoretical force affects particles immersed in the liquid. Clausius–Mossotti factor (3.20) as a function of potential frequency (with parameters of DI water and immersed polystyrene beads with $\varepsilon_p = 2.5\varepsilon_0$ and $\sigma_p = 2.7 \cdot 10^{-4}$ S/m) is displayed in fig. 4.16.

We can see the traveling wave part of dielectrophoretical force which is proportional to the imaginary part of K will be zero for frequencies lower than approximately 500 Hz and negligibly small for frequencies lower than 1kHz – for our experiments we can forget about it. For frequencies lower than 40kHz positive conventional dielectrophoresis will occur, the particles will be pulled to the electrodes.

The dielectrophoretic force acting on a particle can be directly converted to velocity relative to the fluid velocity using Stokes' law

$$\mathbf{F} = 6\pi\eta r\mathbf{u} \;\rightarrow \mathbf{u} = \frac{\mathbf{F}}{6\pi\eta r}, \tag{4.10}$$

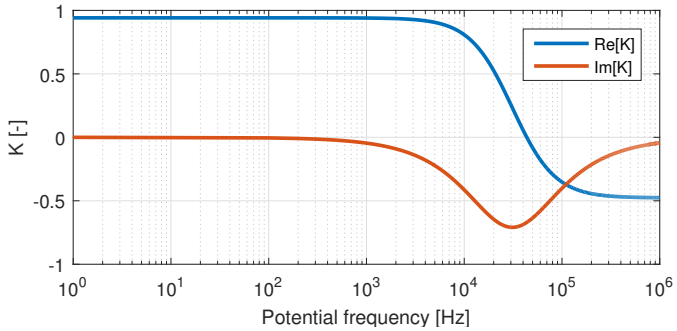

Figure 4.16. Clausius–Mossotti factor for deionized water with immersed polystyrene beads.

with r being the radius of the particle. In literature tracer particles used for measuring the fluid flow are usually fluorescent beads size of 0.5 to 2 µm in diameter. For such particles the velocity caused by dielectrophoresis is lower than 1 µm/s only with exception right at the edges of the electrodes, where the dielectrophoretic force would be the strongest and could possibly trap the particle at place [14].

In our case particles of 15 µm diameter will be used for the experiments. A dielectrophoresis finite element model presented in [29] was merged with the travelling wave electroosmosis model to see how much would dielectrophoretic force influence the particle's movement. For this size of particles the numerical simulations showed dielectrophoretic force significantly affects the particles close to the electrodes. For the liquid bulk, the particle velocity generated by dielectrophoresis is small compared to electroosmotically induced velocity.

A comparison of horizontal velocities from dielectrophoresis and electroosmosis can be seen in fig. 4.17. The parameter remain the same: traveling wave potential with amplitude 5V and 100 Hz frequency. Please note that the final velocity is a sum of these two velocities, since the velocity we get from Stokes' law (4.10) is relative to the fluid velocity.

As we can see close to the electrodes the dielectrophoretic force acting on 15 µm tracer particles does affect the total velocity of the particle very much. The same holds also for vertical velocity presented in fig. 4.18.

4.9 Particle movement

As said few times already, the fluid velocity is estimated through small particles floating inside. A simulation of such movement was also done so we could see the expected movement of our tracer particles. The motion law such small particles obey is a combination of Newton's law and Stokes' law [28]

$$m\mathbf{a} = -6\pi\eta r(\mathbf{v} - \mathbf{u}) + \mathbf{F}, \tag{4.11}$$

where $\mathbf{a}$ is the acceleration of the particle, $\mathbf{v}$ is velocity of the particle, $\mathbf{u}$ is velocity of the fluid (with viscosity η) surrounding the particle, r is the particle radius and $\mathbf{F}$ is force or sum of forces acting on the particle. In scale of micrometer particles the time such small particle needs to accelerate to its terminal velocity is of order of 10^{-6}s. Therefore we can consider the particle moving at its terminal velocity at all times and so we have

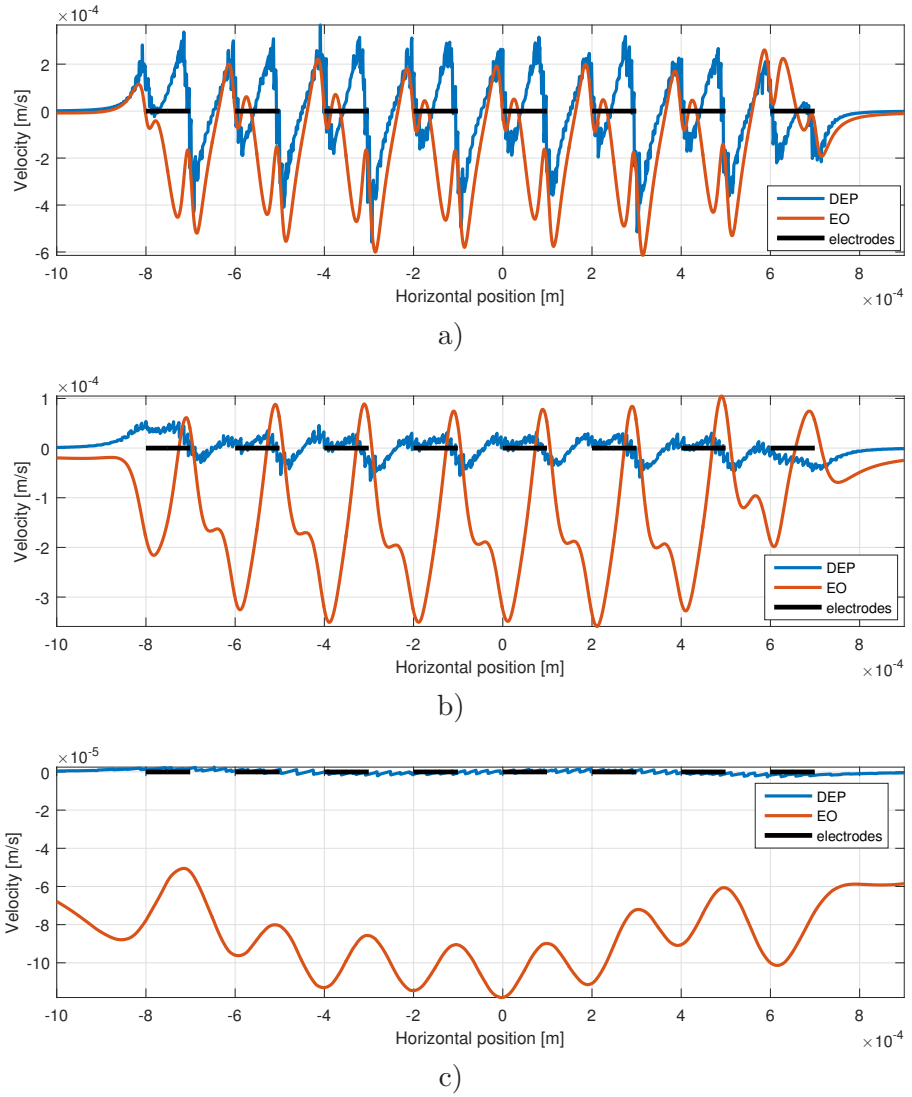

Figure 4.17. The horizontal velocity comparison for traveling wave induced electroosmosis and dielectrophoresis at (a) 20 µm, (b) 50 µm and (c) 200 µm above the electrodes.

$$0 = m\mathbf{a} = -6\pi\eta r(\mathbf{v} - \mathbf{u}) + \mathbf{F}.$$

The velocity of the particle is then

$$\mathbf{v} = \mathbf{u} + \frac{\mathbf{F}}{6\pi\eta r}. \tag{4.12}$$

The polystyrene beads have slightly higher density than DI water. Apart from dielectrophoretic force there is also buoyancy force acting on the particles

$$\mathbf{F}_{\text{buoy}} = \frac{4}{3}\pi r^3(\rho_m - \rho_p)\mathbf{g}, \tag{4.13}$$

where $\mathbf{g}$ is gravitational acceleration, ρ_m is density of fluid (998 kg/m^3) and ρ_p is density of the particle (1050 kg/m^3).

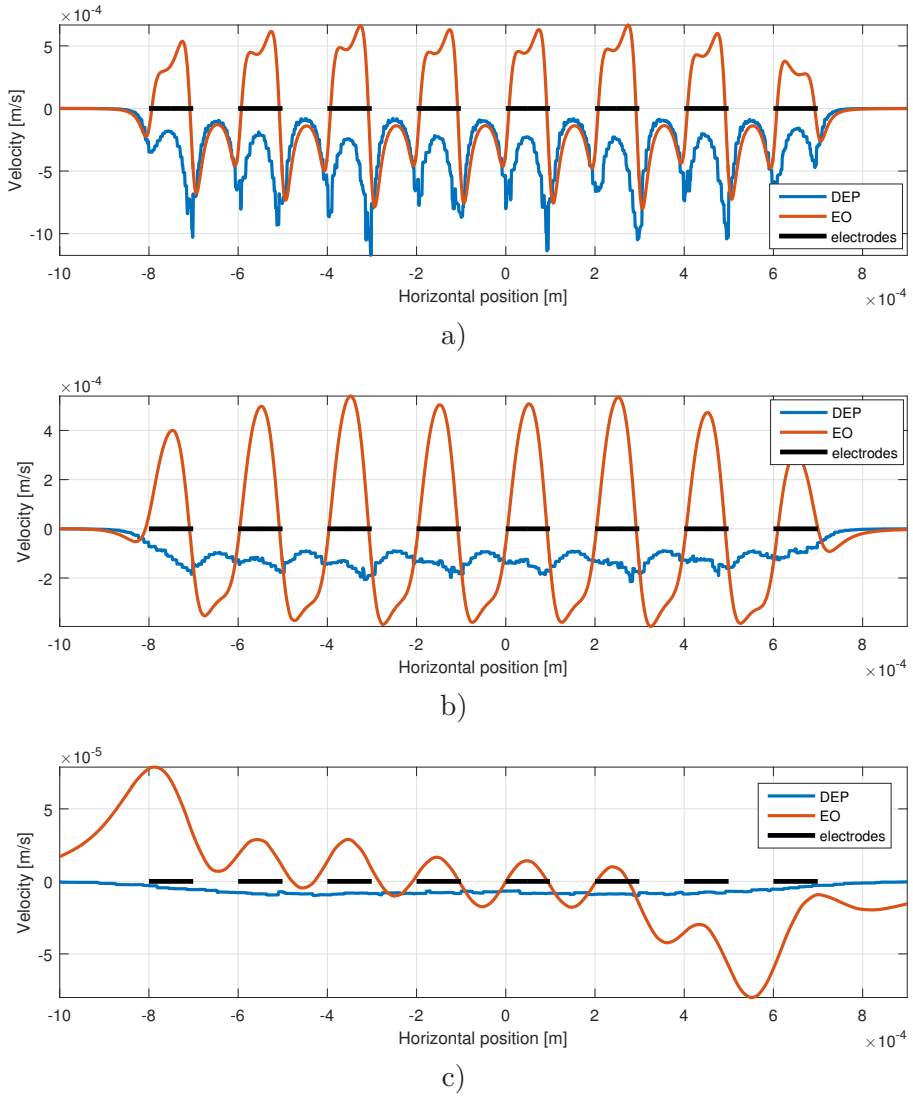

Figure 4.18. The vertical velocity comparison for traveling wave induced electroosmosis and dielectrophoresis at (a) 20 µm, (b) 50 µm and (c) 200 µm above the electrodes.

4.10 Expected particle trajectory

A trajectory of a test particle was acquired doing a time-stepping simulation of the precomputed velocity and force field over the electrodes following a simple procedure:

1. Compute the velocity and force field in COMSOL
2. Interpolate fluid velocity and dielectrophoretic force at the particle's position
3. Compute resulting particle velocity $\mathbf{v}$ according to (4.12)
4. Move the particle in $\mathbf{v}$ direction by distance $\Delta t \cdot \mathbf{v}$ and go back to step 2

Of course this is only an approximation of the particle's movement, but with low Δt the approximation is considered accurate enough. It is also given by the fact the particle reaches its terminal velocity in no time. The time-stepping itself was scripted in MATLAB which was connected to the COMSOL FEM solution via a COMSOL with MATLAB LiveLink application provided by COMSOL.

Movement we expect to see during the experimentation phase is shown in fig. 4.19 (the particle's initial position is right above the second right electrode). Both elec-

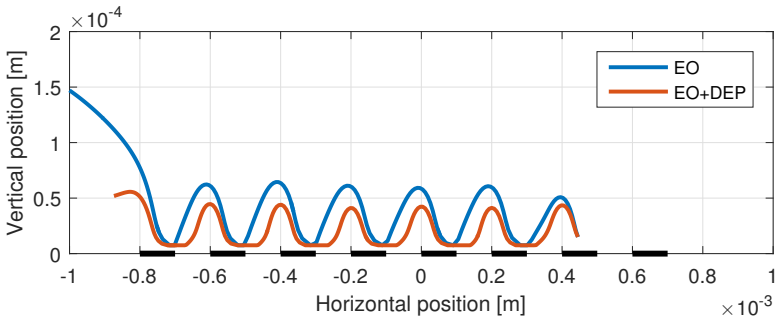

Figure 4.19. Expected movement of 15 µm diameter particle.

troosmosis only and electroosmosis and dielectrophoresis combination induced particle trajectories are presented.

During experimenting it was observed particles can get trapped in little whirls created at the edges of electrodes. There are two factors responsible for this phenomenon. The positive dielectrophoresis force attracts the particles to the edges of the electrodes and also electroosmotic slip velocity changes sign on the surface of the electrodes as well creating those little whirls. An example of particle trapping due to dielectrophoretic force with combination with an electroosmotically induced fluid whirl is presented in fig. 4.20.

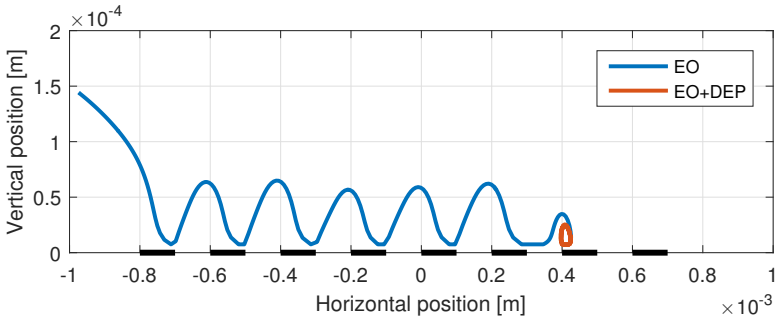

Figure 4.20. Example of particle trapping caused by dielectrophoresis.

4.11 On choice of working fluid

At this point one may ask a question about the choice of working fluid. Deionized water, as the name implies, should not contain ions and therefore there would not be anything to form the EDL from. In theory this might be true, however in reality the DI water contains ions, but in a low concentration. Because of the low concentration, longer time is needed to form the EDL and therefore lower electrode potential frequencies are required. More conductive electrolytes such as KCl solutions would then need a higher potential frequencies for the fluid to experience motion.

The main reason why in this thesis electroosmosis is modeled considering DI water is the preliminary experiments done. As explained in later chapter. No movement was observed for KCl solution. For DI water (which turned out not to be highly deionised, measured conductivity was 10 times higher than standard value) electroosmotic motion was observed.

Deionized water as the working fluid in AC electroomosis was used i.e. in [35], where the authors also discuss the effect of dielectrophoretic force and show particle trapping at the edges of electrodes because of both electroosmotic flow and dieletrophoretic force

as shown in fig. 4.20. In [36] DI water and tap water are used as working fluids, for DI water the authors also use 100 Hz potential frequency.

Chapter 5
Microelectrode arrays fabrication

The goal pursued in this chapter is acquiring microelectrode arrays to perform experiments on. First, the whole fabrication process is described shortly and then we look at each step in greater detail.

5.1 Photolithography

The most common technique for fabricating structures of the smallest dimensions in micrometer scale is photolithography. In general photolithographic method relies on a reaction between a photoresistive material and ultra violet (UV) light. The process is briefly described below with an illustration included in fig. 5.1

1. A selected underlying substrate coated with a conductive material is covered by photoresistive solution.
2. Then it is exposed to UV light. The light might be blocked at some positions by a mask or it can be focused to certain positions by a lens. The difference between these two approaches is discussed later.
3. After the exposure the illuminated substrate is developed in a developer solution, where the photoresistive solution is washed away at positions at which we don't want oru final structure to be conductive.
4. Now the conductive layer not covered by the photoresist is etched away by an acid.
5. At last the remaining photoresistive solution is washed away from the conductive surface.
6. We are left with the structure specified by the our mask design.

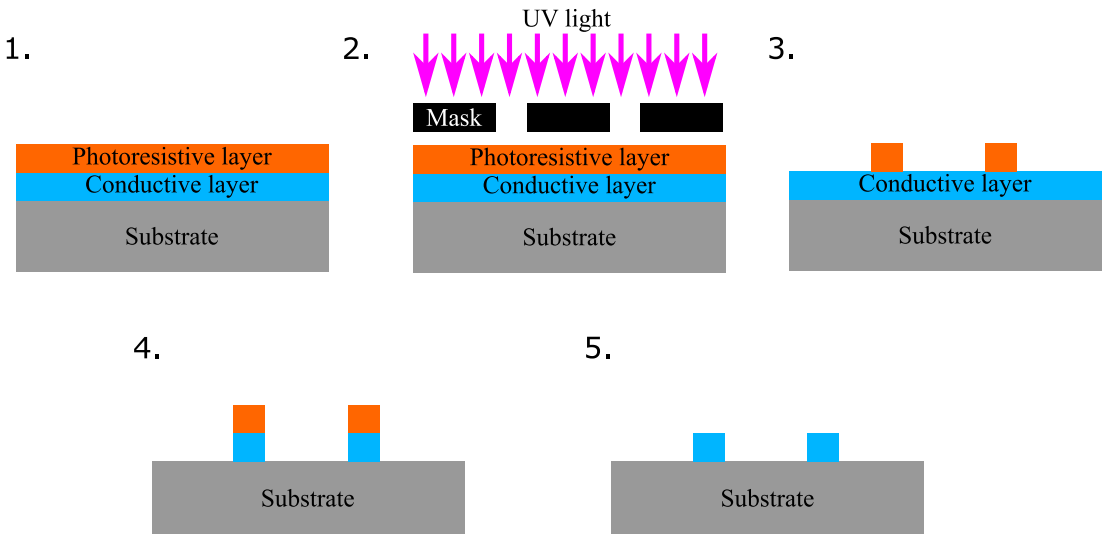

Figure 5.1. An outline of photolithography process.

5.1.1 Substrate material

The most common choice of the underlying material is glass. Glass fulfills the basic requirements – it does not conduct electricity, it does not react with developing solutions and acids used in photolithography and it can easily sustain temperatures of around 150°C. Another viable choice is a plastic foil, for example polyethylene terephthalate (PET). In literature silicone compounds or various types of corundum are also used as an underlying substrate.

Before depositing any material layer over the surface of our substrate it is very necessary to clean the surface as carefully as possible. To clean large particles such as dust and dirt, air pressure is enough. Smaller particles are efficiently removed by putting the substrate into a sonic bath. Acetone can be used to remove other organic contamination. To remove grease and oil isopropyl alcohol is a good choice. A so-called piranha solution (a mixture of sulfuric acid and hydrogen peroxide) is a better choice than acetone and isopropyl alcohol in removing organic residues of the substrate surface. It is however much more toxic and dangerous.

Dipping the substrate into a piranha solution also makes the surface more hydrophilic, which is generally a plus for depositing a conductive layer. Another way of making the surface more hydrophilic is to bake the substrate for a couple of minutes at over 100°C to let water evaporate.

5.1.2 Conductive layer

The material our microelectrode array is actually made of is the material of the conductive layer. As the name indicates it should conduct electricity and it should be easily removable by an etching acid. The most common choices in the field of microelectrode arrays fabrication are gold, indium tin oxide (ITO), platinum and titanium (even though it has much lower conductivity), silver can be used as well. ITO has a great advantage in its color – it is transparent. Also it is the cheapest option from the mentioned materials. However gold is more corrosion resistive than ITO and sticks to the substrate better.

To provide a great grip between the conductive layer and the substrate surface a thin layer is often deposited in the middle. Usually, it is chromium or its compound such as nickel-chromium (NiCr).

The conductive layer is usually deposited on the substrate material by a process called sputtering. During sputtering a so-called target – homogeneous plate of material we would like to deposit on the substrate – is placed inside a vacuum chamber along with the substrate. Then the target is bombarded by ions of a working gas (usually argon) and thanks to the exchange of momentum, the gas ions tear out atoms of the target which land on the substrate (and also on the wall of the vacuum chamber). Sputtering creates a homogenous layer, which is very good for etching the material, since the same amount of time is needed to etch every point over the substrate.

The thickness of the middle layer is usually around 10-50nm and the thickness of the conductive layer is around 150nm.

5.1.3 Photoresistive layer

There are two basic types of photoresistive solution deposited over the conductive layer – positive and negative photoresist. When using the positive photoresist, it should be exposed to the UV light wherever the underlying material is supposed to be removed. With the negative photoresist, the exposure has to be done wherever we would like to keep the underlying material.

It is important to have the photoresistive material spread homogeneously as well. The photoresist usually comes as a fluid. After depositing the photoresist over the substrate with a pipette, the substrate is then put into a spincoater device, in which it spins at a few thousand revolutions per minute. Due to the centrifugal force the photoresist is spread evenly. With the volume of revolutions per minute we can also control the thickness of the photoresistive layer.

After spincoating it is good to bake the substrate with photoresist on a hot plate for about 2 minutes to let water, or other solvent in which the photoresistive polymer is dissolved, to evaporate. However do not heat the substrate too long because the polymer can get damaged by the heat.

5.1.4 UV light exposure

As mentioned earlier, there are more approaches for conducting the UV light exposure. The most common one is exposure through a mask. When using a positive photoresist, parts, where the conductive material is to be kept, have to be blocked by the mask and vice versa for a negative photoresist. The exposure through a mask only takes from around few seconds to a couple of minutes depending on the UV source used.

The second approach is maskless exposure. No mask is placed over the conductive layer covered by the photoresist. Instead, a lens is used to focus the light to a small area. The light is then moved to next area and so on. This exposure, however, takes much more time than the previously explained one. For one 5x7 cm large substrate we are talking of order of tens of hours or even couple of days depending on the detail level in the structure design. Because no mask is needed, this procedure is especially good for prototyping and of course for creating a mask for later use.

5.1.5 Developing and etching

The photoresist is removed wherever we need the design not to be conductive. It is done by immersing the sample in a developing solution and make the photoresist develop itself. The developing solution differs depending on the photoresist used. Further, the sample is rinsed by water and dried with an air pressure. It is also possible to bake the sample for a number of minutes again.

Now we need to remove the conductive layer not covered by the photoresist. This is done by dipping the sample in an acid. Again, depending on the metal used as conductive layer the etching acid differs. It is very important to keep the etching time as short as possible. However, all the material has to be etched away wherever the sample is not supposed to conduct electricity. When etching for too much time, the acid actually starts to attack the material under the photoresist and creates holes in the electrode structure.

Both the developing and etching processes can be interrupted, the solution has to be washed from the sample with water to stop the reaction and then we can examine the results under a microscope or testing the conductivity with a multimeter (for example to see if the electrodes are not connected or if there are significantly large holes in the electrode surface dividing it into two pieces).

After the etching is completed the remaining photoresist is washed away using isopropyl alcohol or acetone. Now we are left with our desired microelectrode array.

5.1.6 Lift-off

There is also a second approach to photolithography. The above explained process is sometimes called subtractive litography. Another way of doing this is called additive

litography or lift-off. During lift-off process the conductive layer actually comes as the last one to be added. We go as follows

1. Deposit a layer of a so-called lift-off resist on cleaned surface of the substrate.
2. Spincoat a layer of positive photoresist.
3. Expose to UV light (through a mask or with maskless technology).
4. Develop the photoresist and hard bake.
5. Wash the lift-off resist away (it should stay intact under the developed photoresist).
6. Deposit the conductive layer.
7. Wash away both resists.

This technique was however not used to fabricate any of the microelectrode arrays used in this thesis.

5.2 Design layout preparation

Both creating a mask for photolithography or performing maskless photolithography require a computer created design layout. Almost any CAD software can be used to draw the design and save it. I used Autodesk AutoCAD for drawing at first, but I found it hard to change the design only a bit – for example to change the width of an electrode (and therefore all the electrodes). In Autodesk AutoCAD drawing is done by hand, so all editing is also done by hand. In the end, OpenSCAD was used for creating the design, because it allows parametric generation of the structure and also can export the file as .dxf. Nonetheless, the designed layout had to be hatched (the outline lines had to be filled with infill to created a „solid" structure), which still had to be done in Autodesk AutoCAD. However the photolithography machines usually demand a layout in .cif or .gdsii format (sometimes .dxf is enough, but there can still be format mismatch errors). To convert .dxf files to .cif or .gdsii a light-weight KLayout layout editor was used.

Two of the layouts created for maskless photolithography can be seen in fig. 5.2. These layouts are designed to fit to a 76 x 52 mm glass slide. To make the fabrication faster, multiple layouts were fitted to one glass substrate. Few layout were also prepared for a small glass slide of dimensions 76 x 26 mm.

In the end of my work on the design I found out about a layout editor software called LayoutEditor which should be able to do all the above-mentioned actions on its own and it does support parametric design. I would therefore advise anyone who would like to design a photolithography layout to take a look at this editor at first.

5.3 Actual fabrication

Microelectrode arrays on which the experiments in later chapter of this thesis were conducted were produced either by me in the lab of Department of Control Engineering (DCE) of CTU in Prague or in cooperation with Institute of Physics of the Czech Academy of Sciences in Praha 8 with myself present, aiding with the process and learning the procedure.

A step-by-step instruction manual for fabrication using maskless photolithography with concrete chemicals and machines used is included in the appendix A.

The instruction manual for manufacturing microelectrode arrays at DCE is printed in [31]. There are however two changes in the procedure. The spincoater program used is now saved under the „static" label (the rpm values are the same). And the exposure

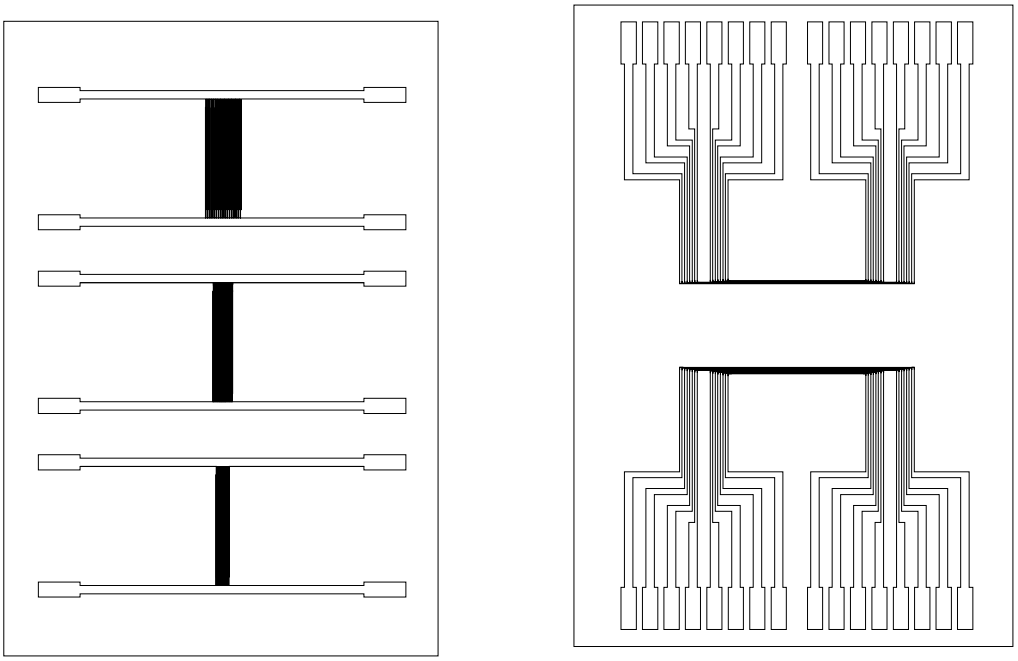

a) b)

Figure 5.2. Layout examples (a) asymmetric electrode arrays consisting of two connectors at each side and 20 microelectrode pairs with different widths in the middle, and (b) symmetric electrode arrays. The outline lines represent the size of the glass slide coated with conductive layer.

time is only 1 minute from about 15 cm distance. The UV light-emitting diode used in the lab has changed since the print of [31]. The chrome mask used for the fabrication with 8 100µm wide electrodes was available for me already fabricated by one of my colleagues.

I used two different underlying substrates. For ITO electrode array fabrication (at DCE CTU) a commercially available PET foil (Sigma Aldrich 639303-1EA, surface resistivity 60 Ω/sq, ITO layer thickness is 72nm) which comes with an already prepared ITO layer on one side covered by a thin plastic foil to reduce dust contamination. The PET foil is very flexible which is both an advantage and disadvantage, because when bending the foil too much the ITO layer breaks very easily.

For maskless photolithography I used a glass slide with 150 nm of gold coated on top of it. Between glass and gold a 50 nm layer of NiCr was added for better adhesion. Both layers were deposited by a Prague company TTS s.r.o.

Also copper coated glass slides were produced at Department of Advanced Materials of Department of Control Engineering at CTU. The adhesion of copper is much worse than the adhesion of gold. This fact was tested experimentally. In the end, copper coated slides were not used for fabrication. I would still like to mention the possibility of fabricating prototype microelectrode arrays using copper coated slides, because copper is a significantly cheaper material than gold. Different chemicals and process timers than mentioned in A would have to be used however.

Following microelectrode arrays were fabricated during my work on this thesis (el.w. stands for electrode width, gap means gap between the electrodes):

- More than a dozen of symmetric 100 µm el.w. and gaps ITO arrays
- One symmetric 50 µm el.w. and gaps gold array
- One symmetric 20 µm el.w. and gaps gold array
- One asymmetric 100 and 50 µm el.w. and gaps gold array
- One four-sector symmetric 100 µm el.w. and gaps gold electrode array

Few trials were made with fabricating asymmetric electrode arrays, all of them except for one turned out defected. Various electrode widths (ranging from 10 µm to 100 µm) as well as gaps between the electrodes (in the same range) were tested. Microelectrode arrays with dimensions lower than 50 µm were fabricated with multiple shortcuts between the electrodes. These shortcuts could not be removed in such way the electrode array would be usable anymore.

Even though the thickness of the ITO layer used (72nm) was about half the thickness of the gold layer used (150nm), the electrical parameters for both arrays differed significantly. For ITO microelectrode array of a minimum width of conductive structure 100 µm the resistance over the electrode was about 20-25 kΩ. This value did strongly depend on the quality of the fabrication process. If the electrodes did not have sharp edges or had holes in them (without interrupting them) their resistivity increased significantly (to even 50 kΩ and more). On the other hand, the resistance over the gold electrodes was in range of 100-500 Ω even for electrodes of 20 µm width.

5.4 Other viable fabrication methods

5.4.1 Inkjet printing

Another possible method for creating small-scale structures is inkjet printing. A printhead deposits a small droplet of conductive material in liquid form, e.g. gold or silver, on the surface of the substrate. This deposition repeats in a predefined grid of points. The gap between individual grid points or the time delay between two droplets deposition are parameters the user has to tune.

Few deposition test were carried out for us in materials laboratory at CTU in Dejvice with electrode array design created for photolithography, but even 100 µm electrodes with gaps of the same width were found difficult to fabricate with this method. With only 100 µm gaps between printed lines, the droplets of the metal had different contact angles with the surface and it was observed two or more droplets merging into one creating shortcuts between the electrodes. More on this particular method can be found in [37].

5.4.2 Electric discharge machining

During electric discharge machining also known as spark machining, a material is being removed from a prepared sample one layer at a time using sparks coming from an electrode. Generated heat is the cause of sample material evaporation and removal. The material which is being removed has to be electrically conductive.

Even micrometer scale applications are possible with this technique. For example, in [38] the authors present a microscale electrode array for measuring brain activity.

For design such as ours extremely small spark electrodes would have to be fabricated. Unfortunately, I did not find any way of how to try this method in Prague.

5.5 A note on 3D structures fabrication

A 3D microelectrode structure as described in chapters 3 and 4 could be fabricated by multiple iterations of photolithography. After we are done with one height level of our design the cycle is repeated from the start. For the 3D electrode design where there are only 2 height layers 2 photolithography cycles would have to be done. There is a risk in the alignment of the second layer however. For micrometer scale structures a few microns of error in calibration of the position of the sample could ruin the whole process. Also, twice as much waste material is generated.

Also electric discharge machining technique is capable of delivering 3D microelectrode structures.

5.6 Fabrication contacts acquired

Various Czech institutions were contacted in order to negotiate a partnership to fabricate or help fabricate a few prototype microelectrode arrays. As a documentation of all the possible means in outsourcing some of or all of the fabrication steps described in this section for anyone who would like to continue in this work the contacts acquired are attached in Appendix C.

Chapter 6
Experiments

In this section, experimental results are presented. The experiments were performed using microelectrode arrays fabricated according to the methods presented in the previous chapter.

6.1 Description of the experimental setup

Illustrative sketch of the experimental setup is shown in fig. 6.1. The electrode array is connected via either 30 pin connector (PET + ITO microelectrode arrays) or multiple 8 pin clip-on connectors (gold arrays) to a signal generator. Two different signal generators were used.

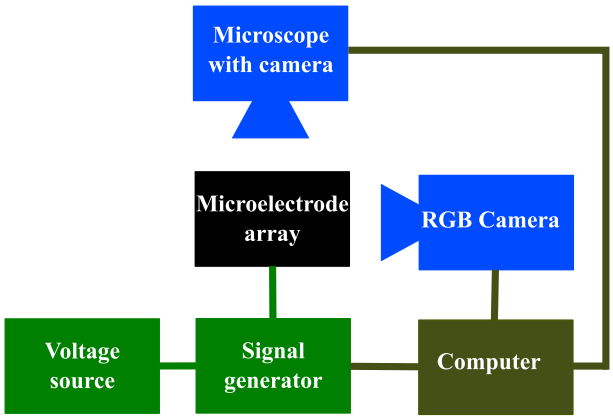

Figure 6.1. Experimental setup illustration.

The first one was a product of one of my colleagues for powering a microelectrode array my colleagues used for dielectrophoresis experiments. This generator takes input voltage from an ordinary table voltage source and outputs multiple phase-shifted square waves with peak-to-peak amplitude equal to the input voltage. The phase shift and frequency are set in MATLAB environment. Max peak-to-peak amplitude of this generator is 50 V and the frequency range is 50 Hz - 312 kHz.

The other signal generator used was a commercial PC data acquisition card Humusoft MF624. This card has 8 analog outputs which can also be controlled through MATLAB. It only allows a maximum peak-to-peak amplitude of 10 V, however, allows us to use any signal shape we like – e.g., sine wave instead of a square wave.

Two cameras were used for observing the microelectrode array. From above I watched the measurement scene through a microscope with an Allied Vision Pike camera mounted to it (an installation guide for the camera and how to get it working in MATLAB is included in appendix B). Side view was acquired by e-con systems See3CAM 10CUG CB camera.

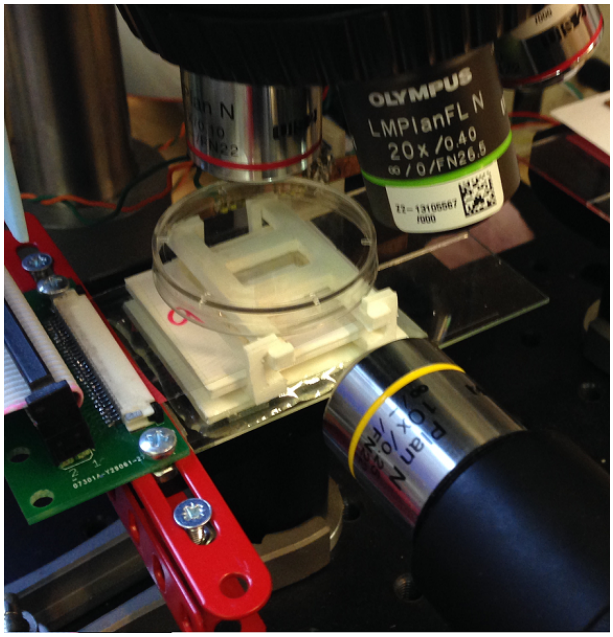

Figure 6.2. Experimental setup with ITO microelectrode array.

The fluid itself is contained in a small pool made of PDMS (Polydimethylsiloxane, a polymeric organosilicon compound prepared by mixing an elastomer and a curing agent in 10:1 ratio). This mixture is then poured into a form. The form used was fabricated by sticking glass slides together with epoxy glue, forming an empty block. Then a small solid block was placed in the middle so the pool would have an empty volume to contain the liquid. The form can also be printed on a 3D printer, but because the walls of 3D printed plastic are not as smooth as glass walls the PDMS loses its see-through property. On the other hand 3D print is much quicker than sticking glass slides together (the glue also has to harden). 3D printer form fabrication is therefore a better choice when observing the fluid domain from above. When also using a side view camera, which looks at the scene through PDMS walls, the pool has to be fabricated using glass form.

The silicon polymer forms only the walls of the pool. From top it is freely accesible and from bottom there is the microelectrode array. The close-up picture of the setup with ITO array is presented in fig. 6.2. The PDMS pool is held in place by a flexible plastic structure printed on a 3D printer.

6.2 Solution conductivity stability

Before introducing the actual experiments I will briefly talk about two limits which I encountered. The vast majority of experiments was done using a deionized water. However, the results differed one from another quite a lot. Lately I have figured out the conductivity of DI water is not really constant and varies a lot over time even in closed plastic containers. To see how much does the conductivity differ with time a simple measurement using Jenwey 4510 conductometer was done.

One important result was the conductivity of DI water coming from the Direct-Q 3 UV machine is ten times higher (50 µS/m) than a standard value for DI water conductivity (5.5 µS/m). After two hours the conductivity of prepared DI water doubles. One has to bear this fact in mind when performing experiments. For this reason, the DI water used for experiments was changed after each experiment – every 5 to 10 minutes.

Conductivity measurements were also performed on stronger electrolytes such as NaCl and KCl solutions which showed as stable. Their conductivity (in order of mS/m) was not changing over a period of few hours.

6.3 Potential/frequency limits

The second limit I came across during the experiments is a limit in both input potential and frequency. For too high potentials and/or too low frequencies the electrode arrays (both ITO and gold) started to decay very fast. Probably some kind of electrolysis could be seen over the electrodes. For 10 V peak to peak potential amplitude and 50 Hz frequency, the ITO electrodes got destroyed in seconds. The destroyed ITO electrodes can be seen in fig. 6.3 a). For the gold electrodes, the same potential caused damage as well. Over the gold electrode array visible bubbles were observed, after few seconds the whole areas of the electrodes started to lift off from the surface. The bubbles which stayed over the gold electrodes even after turning the potential off are shown in fig. 6.3 b). The lifted electrode is marked in red.

From the experiments there seems to be a ratio between the potential frequency and amplitude, which does damage the microelectrode arrays, this ratio was however not estimated.

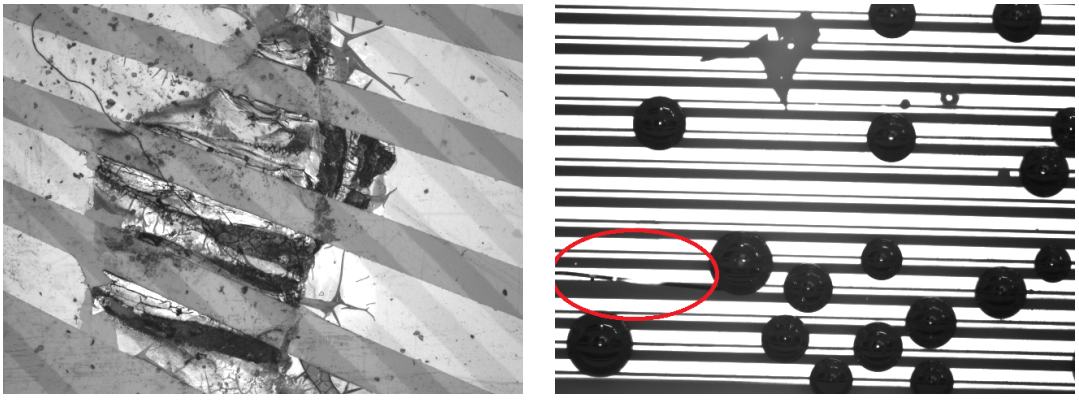

a) b)

Figure 6.3. Destroyed electrode arrays by electrolysis.

6.4 Particle image velocimetry

For measuring a fluid velocity particle image velocimetry (PIV) is a well known and the most spread technique. As mentioned in chapter 3 the velocity is estimated by measuring positions of small particles floating in the fluid.

There are some existing solutions for PIV such as OpenPIV [1] for MATLAB or Python and Mosaic particle tracking software for ImageJ [2].

However, after running a few experiments with the existing solutions I decided the easiest and the most user-friendly way of analyzing my experiments would be scripting my own heuristic particle tracker. The polystyrene beads are transparent and over the ITO microelectrode arrays they are visible as black dots thanks to bending of light coming through them to the microscope. Tracking a black dot was done using a region

[1] http://www.openpiv.net/openpiv-matlab/
[2] http://mosaic.mpi-cbg.de/?q=downloads

of interest and finding the darkest pixels. This approach was successful when tracking multiple not touching particles at speeds less than 200 µm/s. For higher speeds hand estimation had to be used. For comfortable and easy hand annotation a simple graphical user interface was created in MATLAB.

Over the gold microelectrode arrays the particles were not well visible anymore, because gold is not transparent as ITO and reflects more light. For most of the velocity measurements over gold electrodes hand particle position estimation had to be done.

6.5 Measured velocities

Particle velocities were measured using the microscope-mounted camera. The velocities in pixels/frame were recalculated to µm/s through a constant acquired empirically through measuring the distance in pixels between the outer edges of the outer electrodes. This distance corresponds to 8 times electrode width + 7 times gap between two electrodes. The velocities measured for different microelectrode arrays are presented in tables 6.1, 6.2 and 6.3. Traveling wave potential over a symmetrical array of microelectrodes was used for measurement experiments. For each pair of potential amplitude and frequency there are the minimum and maximum particle velocity measured. There are some data from high peak to peak potential missing from table 6.3, these data were not measured because of a possibility of destroying the array as explained in section 6.3.

Computing instantaneous velocity from particle's movement over few frames of recorded videos produced a high variance in the data. Therefore the velocities measured are average velocities over distance corresponding of multiple electrode widths and gaps between the electrodes. Distance traveled s by the particle is know and time t it took is also know because of the constant framerate of used camera, average velocity is then simply $v = s/t$.

Because of repeatability of the measurements, the velocities were measured for particles which were touching the ground surface (electrode itself or PET foil or glass). The height of the surface level of our pool was about 1 to 1.5 mm and it took the particles time in order of seconds to few tens of seconds to fall to the ground level because of gravity (or downwards buoyancy, the particles are denser than water). In this case, no initial vertical coordinate of the particle had to be evaluated.

Frequency\Amplitude	3 V_{pp}	4 V_{pp}	5 V_{pp}
100 Hz	No net flow	157.72 193.24	198.05 250.94
200 Hz	50.48 63.55	118.94 141.73	205.85 322.94
300 Hz	No net flow	No net flow	125.87 139.27
400 Hz	No net flow	57.42 72.4	113.59 115.21

Table 6.1. Particle (15 µm diameter) velocities (in µm /s) measured for gold symmetric microelectrode array with electrodes of 50 µm width and 50 µm gap.

Frequency\Amplitude	3 V_{pp}	4 V_{pp}	6 V_{pp}
100 Hz	No net flow	13.81 34.71	No data
200 Hz	27.78 78.60	8.44 15.24	510.72 530.11
300 Hz	45.89 60.61	No net flow	181.40 381.93
400 Hz	No net flow	no net flow	223.49 323.88

Table 6.2. Particle (15 µm diameter) velocities (in µm /s) measured for gold symmetric microelectrode array with electrodes of 20 µm width and 20 µm gap.

Frequency\Amplitude	3 V_{pp}	4 V_{pp}	5 V_{pp}	6 V_{pp}	7 V_{pp}	8 V_{pp}
50 Hz	No net flow	26.23 27.68	19.01 32.05	80.70 107.64	94.30 103.45	137.74 141.2
75 Hz	No net flow	No net flow	51.06 75.8	74.5 93.04	No data	No data
100 Hz	No net flow	No net flow	No data	65.1 73.6	No data	No data

Table 6.3. Particle (15 µm diameter) velocities (in µm /s) measured for ITO symmetric microelectrode array with electrodes of 100 µm width and 100 µm gap.

6.6 Asymmetric microelectrode array

Only one asymmetric microelectrode array was fabricated without flaws – gold 50 µm and 100 µm electrodes separated with gaps of the same widths. Measurements with the same frequencies and amplitudes as displayed in tables 6.1, 6.2 and 6.3 were carried out. No net movement was however observed. The particle trajectories were chaotic, mainly getting stuck in large whirls over the electrodes.

6.7 Experiments discussion

Even though some data were measured and shown the experiments did not go well. Sometimes (especially at lower frequencies and higher voltage amplitudes) the particles experienced a rather chaotic movement. Also, the measurements were really unconsistent. Even though the deionized water the particles were immersed in was changed very often, on two different days with the same microelectrode array the results did differ – for example a frequency/amplitude pair would produce a net flow and on another day no net flow was observed. This was true especially for the ITO arrays where for some arrays I could not see any movement at all. The arrays were not interupted and the signal was checked with an oscilloscope, but still no movement was visible.

I found the experiments extremely unreliable. In future, if someone would like to continue with my work, the experiments should be revisited and the unpredictability should be dealt with. In literature addressing electroosmotic pumping usually larger number of parallel electrodes is used (20 and more), maybe, larger number of electrodes would decrease experiment unreliability.

In this thesis, 8 parallel electrodes are used on the symmetrical arrays and 20 microelectrode pairs are used on the one asymmetric microelectrode array fabricated. The reason why 8 electrodes were chosen was simple connectivity. The idea was to test electroomosis on a simple layout and when successful, continue with fabricating larger and more complicated layouts.

6.8 Potassium chloride experiments

In literature reviewed the most common liquid used for experiments with electroosmosis is potassium chloride (KCl). A solution of KCl with conductivity of about 1.8 mS/m was prepared and tested. No movement could, however, be seen over neither the ITO microelectrode array or the gold arrays. A frequency range of 50Hz to 50kHz was tested with peak to peak voltage ranging from 1 V up to 20 V. No visible movement of the particles at any height over the microelectrodes was observed.

The main motivation in using deionized water in this thesis is I got to get at least some of the motion measurements using DI water, it is fast and easy to prepare at the same quality each time (I took it from Direct-Q 3 UV purification device) and as a plus it is also suitable for dielectrophoretic micromanipulation.

In theory, KCl solution should need higher potential frequency (about 0.1 to 20kHz depending on the concentration) to experience electroosmotic motion. As said already this was not confirmed during the experiments.

6.9 Thin insulating layer

Multiple research papers also suggest covering the electrodes with a thin insulating layer to prevent electrolysis from happening. I did experiments with covering the arrays with an insulating photoresist which was then exposed to UV light and developed. The thickness of such layer was measured with a profilometer as about 2 µm.

The layer stopped electrolysis from happening and the microelectrode arrays did not get damaged as menitioned in section 6.3. On the other hand, no visible movement of the particles was observed for neither DI water nor a KCl solution.

6.10 Model validation

Experimental particle velocities acquired from recorded video data were compared with data acquired from the mathematical model created. Because we have measured an average velocity, we have to compare it with similar data. Therefore particles movement paths were simulated by an already explained (section 4.10) time-stepping method.

Comparison of mathematical model data and experimental data is shown in fig. 6.4. Parameters used for the numerical simulation are shown in table 6.4. The conductivity of deionized water σ was changed to the measured values and therefore the Debye length had to be recalculated according to (3.4).

It is clear the model does not represent the data acquired with the ITO array well. This difference only emphasizes the observed behavior. The velocity measurements, especially for the ITO array, were not consistent in time. For velocities measured on the gold array, the model is very near the real data. However, it is true only for the

Parameter	Symbol	Value	Unit
Diffusivity	D	$2 \cdot 10^{-9}$	$m^2\ s^{-1}$
Relative permittivity	ε	80	-
Conductivity	σ	$80 \cdot 10^{-6}$	S/m
Debye length	λ_D	120	nm
Capacitance ratio	Λ	0.25	-
Dynamic viscosity	η	$1.002 \cdot 10^{-3}$	Pa s

Table 6.4. Deionized water parameters used during validation.

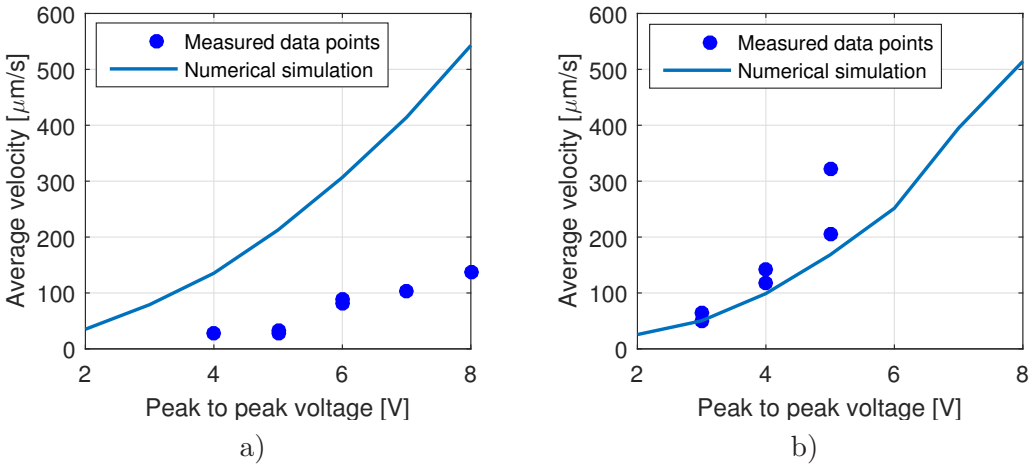

Figure 6.4. Measured results compared to numerical simulation, (a) ITO symmetrical array (100 µm el.), $f = 100Hz$, (b) Gold symmetrical array (50 µm el.), $f = 200Hz$.

200Hz frequency data. The velocities predicted by the model had an error between 60 to 120 percent for the other data points measured over the gold arrays.

The shape of induced velocity field observed through the side camera was the same as presented in the mathematical model in section 4.7.

We could get a better fit of the ITO microelectrode array data with tuning the parameters of the model. For example the ratio between Stern and diffuse layer capacitance Λ is not very well known in the current state of the art of electroosmosis theory, the value of 0.25 is a good guess as stated in literature [14]. Changing this ratio would change the average velocity linearly. Also the value of Debye length λ_D is not a measurable fact (at least at this moment) and it is more of an approximation. Lowering λ_D increases the electrical double layer capacitance and also the average velocity. Unfortunately, tuning the parameters to get a fit for one data made the other data not fit the model. The model parameters, therefore, were not the problem. The model itself, however, can not be said to be wrong only because it does not fit the data, because the data are very unstable and unreliable.

During the measurements some particles got stuck in the fluid whirls or dielectrophoretic traps at the edges of the electrodes as explained in section 4.10. This fits the created model and the same behavior can be seen in model experiment shown in fig. 4.20. However, when the particle started to move and crossed about 2 widths of an electrode of distance it did not get trapped. For this reason, the effect of dielectrophoresis was lowered to acquire data presented in fig. 6.4.

Some of the particles also got stuck and did not move at all. This might be because of the particle sticking to underlying foil or glass. Also, particles did stick one to each

other. In [17] the authors dealt with the same problem and they suggest to presoak polystyrene beads to 0.1% pluronic solution to reduce their stickiness.

Qualitatively the mathematical model presented in this thesis fits the observed behavior. The tracer particle's motion fits the model in its trajectory, but the measured velocities are not predicted correctly for all the measurements.

Chapter 7
Control

In this chapter, I propose three methods for controlling fluid flow using the arrays of microelectrodes. Because of problems with the experiments described in the last chapter, the methods are tested using the mathematical model.

7.1 One-dimensional on-off control

The simplest microelectrode geometry is a parallel configuration. When using symmetrical electrodes and traveling wave potential, the fluid flow direction can be switched by flipping the direction of the potential wave. Working on this presumption a simple on-off control using one potential frequency and amplitude was implemented. The particles' motion is simulated using an already presented time-stepping method. The control takes place only in a 2D plane since fluid flow in the direction of the largest length of the electrodes is negligible. This fact was confirmed in the mathematical model as well as during experiments.

The control law is as follows, for electrode phase shifts, starting from the leftmost electrode, 0, $\frac{\pi}{2}$, π, $\frac{3\pi}{2}$, 0, ..., the particle (and of course the working fluid as well) experiences motion from the right edge of the electrode array to the left one. When we flip the phase shift vector, the induced motion also flips direction. Therefore the phase shift vector applied to the electrodes depends on the desired direction which is computed as desired position $\mathbf{p}_{\mathrm{DES}}$ minus current position $\mathbf{p}_{\mathrm{CURR}}$.

One problem I dealt with making this simple control law was the trapping of particles at the edges of electrodes. With 15 μm particles, the trapping occurred very often. This problem was not observed during the experiments in such quantity. To overcome this inconvenience, particles with smaller diameter (5 μm) were chosen.

The computational domain for such control experiment was set to the real problem I was dealing with during the experiments – a small pool of DI water. Therefore the left and right hydrodynamical boundaries of the domain are set as walls. Fluid flow right above the electrodes is not affected by this change, however, in the upper half of the pool the fluid moves in the opposite direction than the fluid right above the electrodes as it needs to recirculate to satisfy the continuity equation.

The control result is shown in fig. 7.1 and 7.2. In fig 7.2 the higher y-axis limit is set to 200 μm. The height the considered domain was 1.5 mm, but the motion took part in the lower part only. For 5 μm particles, this control scheme works well, for 15 μm particles it is not reliable and fails quite often.

7.2 Two dimensional on-off control

Until now we only had parallel electrodes all with the longest dimension in one direction. A bit different microelectrode setup with four sectors of electrodes was also inspected. The same idea is also used for dielectrophoretic manipulation [39] [30]. With an electrode array shown in fig. 7.3 a 2D manipulation with micro objects as well as

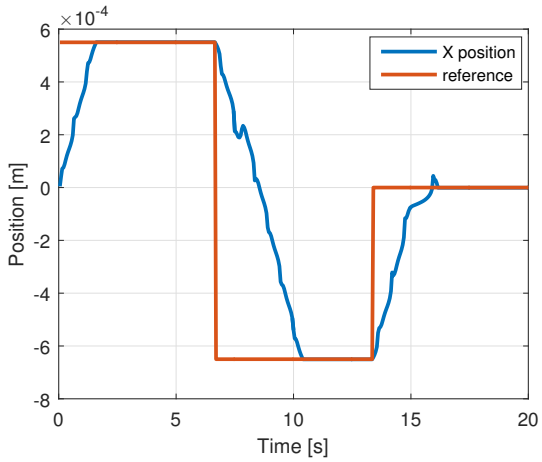

Figure 7.1. X position of the particle in time.

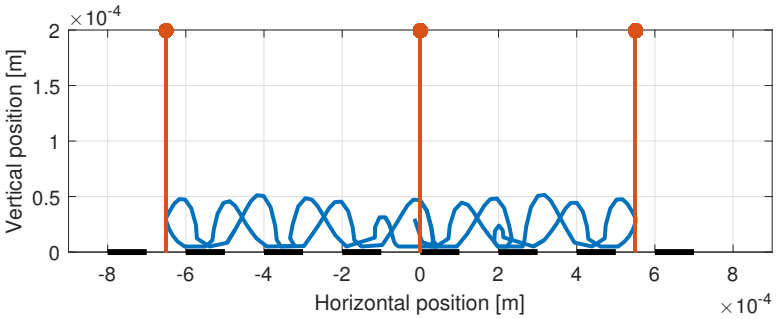

Figure 7.2. Trajectory of the particle. The orange points and lines represent the individual goal position references – the reference is given only as a horizontal coordinate.

four directional fluid flow control might be achieved. Or at least that is the goal. A similar idea is also sketched in [40].

Microelectrode with presented geometry and with electrode width 100 µm and the same gap between the electrodes was also fabricated as documented in chapter 5.

The idea is to run 4 separate traveling potential waves, each one on one set of the electrodes. With changing the direction of the traveling wave, the fluid flow over this part of the middle sector will change direction. A COMSOL model with a hypothetical valve microstructure over it was created and it is shown in fig. 7.4 The initial control idea was to actuate the working fluid through the microchannels in the corners using planar electrodes in the middle part. This way a controllable 4-way valve could be created.

Various control strategies were tested and it was proven the valve fluid flow velocities through the input microchannels can be controlled using the planar electrodes. The input (or output) flows are however not independent one of the other, which is partly because the continuity equation has to be fulfilled. Three successful control strategies are shown in fig. 7.5. The red arrows represent fluid flow direction and are acquired as a FEM solution, the blue arrows represent direction of the traveling potential wave (in terms of phase shifts the direction is from left to right 0, $\pi/2$, π, $3\pi/2$), the electroosmotic slip direction is then opposite the traveling potential wave direction.

In 7.5 a) one microchannel was selected and all the fluid flow through the valve was directed through it, in 7.5 b) and 7.5 c) two microchannels were selected as output microchannels. The maximum fluid flow velocity through a microchannel in scenario

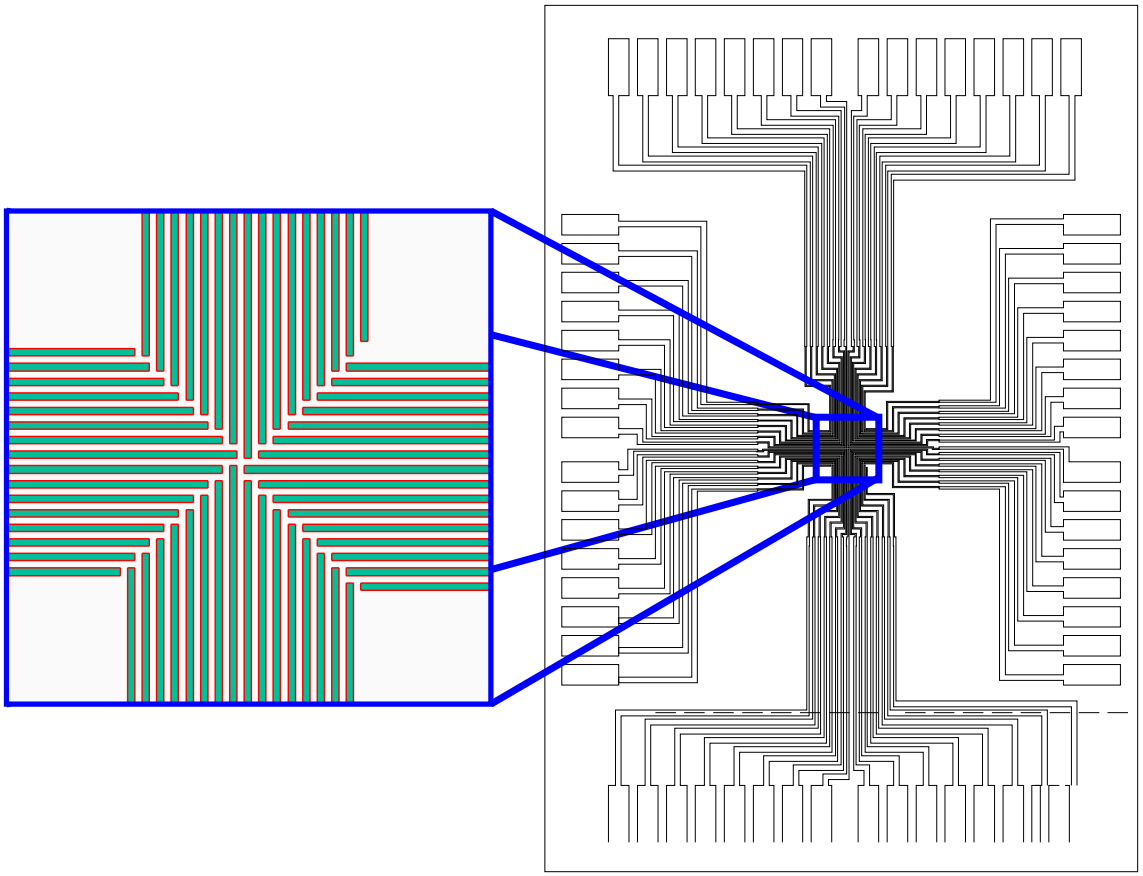

Figure 7.3. Four sector microelectrode array layout and zoom of the middle part used for flow control.

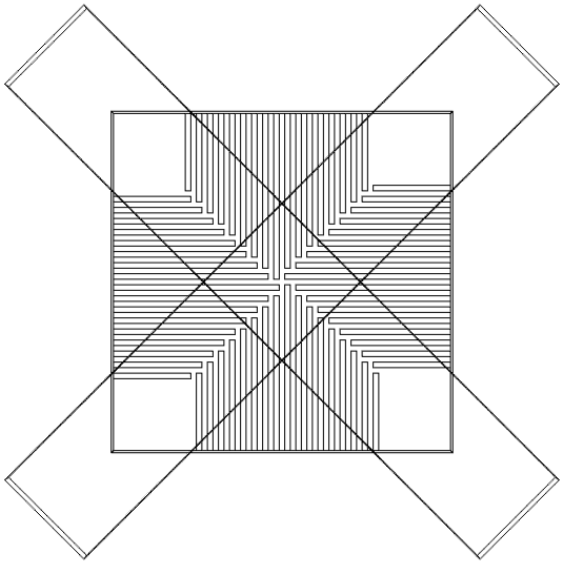

Figure 7.4. Four sector microelectrode array 3D COMSOL model (viewed from above). The four microchannels form a proposed 4-way programmable valve.

7.5 a) with 5 V potential amplitude and frequency of 100 Hz was about 45 μm/s. In 7.5 b) and c) the fluid outflow velocity was roughly a half of that in 7.5 a). DI water as the working fluid was considered.

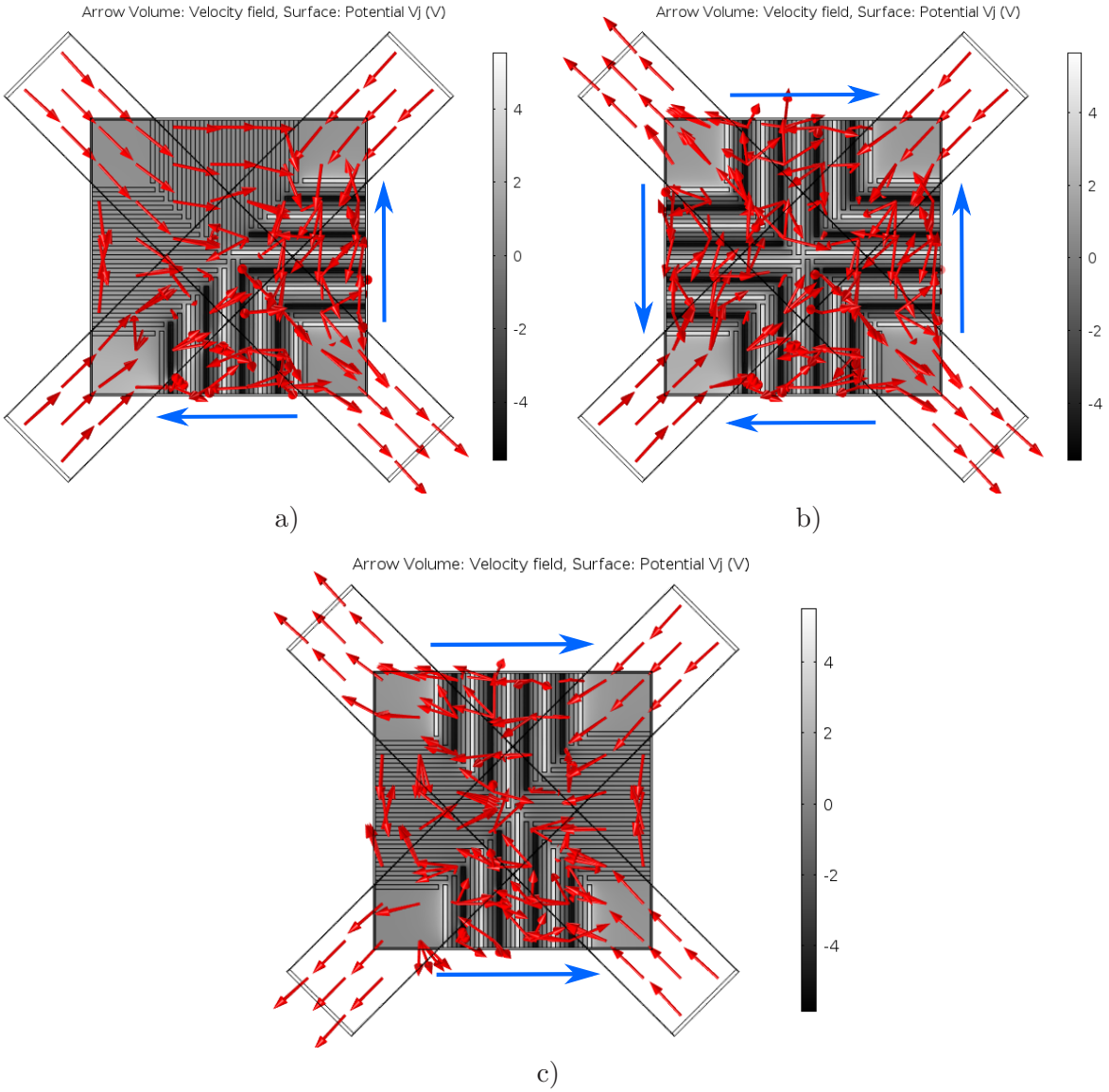

Figure 7.5. Four sector array valve control strategies.

The four-sector array shown in fig. 7.3 was also fabricated and the control strategies proposed were also tested. Since there is currently no possibility of microfabricated closed structure such as the one shown in fig. 7.4 a square PDMS pool was used again. Because of the problems discussed in the last chapter, however, no net fluid flow was observed over the individual microelectrode sectors.

7.3 Optimization based control

The third approach for fluid flow control and also control of a particle is inspired by [41]. The basic idea is to use electroosmosis as a microchannel pumping mechanism in multiple microchannels. These microchannels are connected to one larger area where the actual motion takes place. Such design with six microchannels is shown in fig. 7.6

7.3.1 Data preparation

To control fluid field inside the middle domain, fluid flows at the individual channels have to be controlled. To derive a control strategy, we are going to need n basis, where

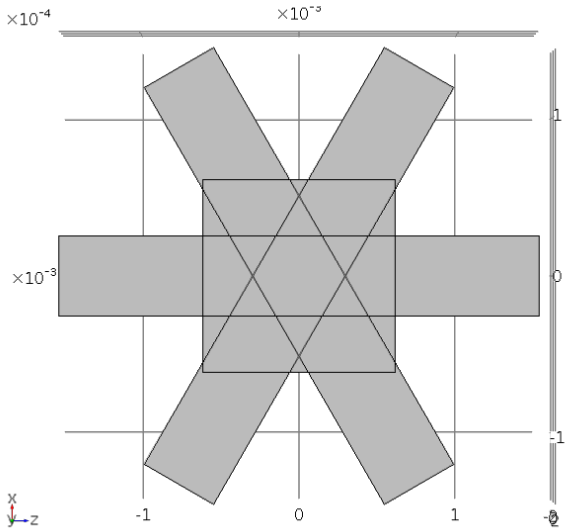

Figure 7.6. Control domain design. This is a 2D projection, the design is a 3D structure.

n is the number of microchannels. Each such base is created by numerically simulating a fluid flow inside the whole domain with only one microchannel pumping velocity in one direction with predefined pumping speed which is constant for all bases. The other microchannels are set as closed. The solution is then split into a dense grid of points in which it is evaluated and saved. This procedure has to be repeated for all microchannels, creating n basis data sets. Creating all these data sets might even take up to days depending on the geometry of the model and the mesh, the upside is it has to be computed only once for a selected domain geometry. The basis data sets look like it is shown in fig. 7.7.

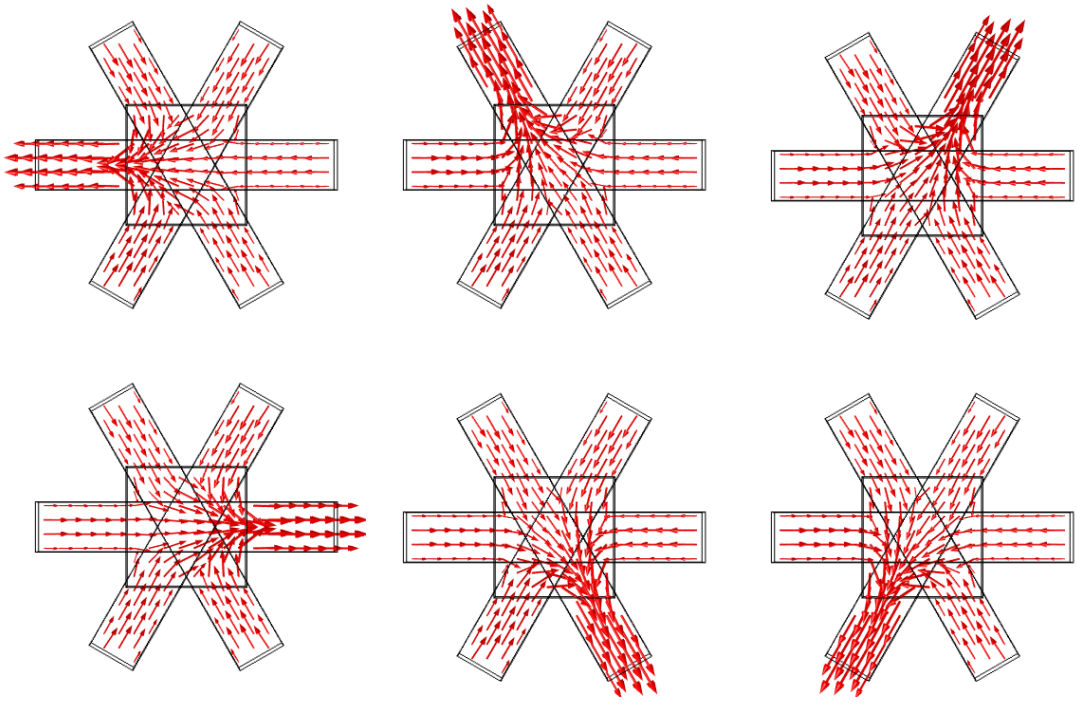

Figure 7.7. Basis data sets illustration.

With these data prepared beforehand, the control itself is then only about solving a linear system of equations. There is no differential equation to solve because we neglect inertia of the particle and assume it is always traveling at its finite velocity. Also, inertia of the fluid is neglected, and therefore we consider the Navier-Stokes equation (4.4) to be linear. Both these assumptions are explained earlier in this thesis, namely in chapter 4. The Navier-Stokes equation linearity is essential for the use of this proposed algorithm.

7.3.2 Control problem statement

Now how do we assemble the system of linear equations to solve. We observe our particle at certain position **p**. Then we look into our set of basis data and we assemble matrix

$$\mathbf{A} = \begin{pmatrix} u_1 & u_2 & \dots & u_n \\ v_1 & v_2 & \dots & v_n \\ w_1 & w_2 & \dots & w_n \end{pmatrix}, \tag{7.1}$$

where u_i is an x coordinate element of velocity vector of velocity field of i-th basis function at the particle's current position, v_i is y element and w_i is z element of the same velocity vector. We also assemble vector b as

$$\mathbf{b} = K(\mathbf{p}_{\mathrm{DES}} - \mathbf{p}), \tag{7.2}$$

where $\mathbf{p}_{\mathrm{DES}}$ is a desired position of the particle and K is a scaling constant, which is in the formula to assure reasonable desired velocity. Vector **b** represents desired velocity of the particle and therefore desired velocity of the fluid flow at point **p**.

The linear system we would like to solve is then

$$\mathbf{Ax} = \mathbf{b} \tag{7.3}$$

where **x** is our unknown vector. Individual elements of this vector represent a multiplier. The desired fluid flow through i-th microchannel is then x_i times the inlet fluid flow used for computing the i-th basis data set. For example, if the basis data sets were generated using 50 µm/s average pumping speeds, vector

$$\mathbf{x} = \begin{pmatrix} 3 \\ 2 \\ 1.5 \\ 1 \\ -5 \\ -2.5 \end{pmatrix}$$

tells us we need to set 150 µm/s average pumping speed at microchannel 1, 100 µm/s at microchannel 2 and so on. To satisfy continuity equation, sum of all inlet velocities should sum up to 0. This means adding a row of ones as the last row of **A** and adding a zero as the last element of **b**. Experimentally it was show sometimes this is hard to achieve when numerically evaluating (7.3), the average inlet flow velocities do not sum up to exact 0 and FEM solution is then very slow or even fails to converge. To overcome this problem, we can treat one of the microchannels as an open boundary (for example the one farthest from particle we would like to control). Therefore we only have $n - 1$ microchannels to control and we do not have to sum all the flows throught them to 0.

7.3.3 Solutions using MATLAB

To solve (7.3) two ideas were tested. The system (7.3) is underdetermined (we have more than three input microchannels), therefore if there is some solution, there are infinitely many solutions. In MATLAB two options for solving such systems exist

$$\mathbf{x} = \mathbf{A}^{+}\mathbf{b},$$

where + subscript represents pseudoinverse operation. In MATLAB words:

```
x = pinv(A)*b
```

This command minimizes the (Euclidean) norm of $\mathbf{x}$. The solution computed has the lowest norm of any other solutions. The second option for solving an underdetermined system in MATLAB is using the backslash command:

```
x = A\b
```

In this case $\mathbf{x}$ has the lowest number of non-zero elements as possible. Both of these solutions have a problem they are not bounded in any way. Even though the pseudoinverse solution has the lowest norm possible, it might result in a set of average inlet velocities which are not achievable by our system. To solve this trouble a heuristical scaling was done. The resulting $\mathbf{x}$ vector was scaled so that the highest number will correspond to the highest average pumping speed achievable.

The second approach to solving (7.3) for $\mathbf{x}$ is to formulate an optimization problem. The function to minimize is of our choice. Following optimization problem was solved,

$$\begin{aligned} \text{minimize } & \mathbf{x}^T\mathbf{I}\mathbf{x}, \\ \text{subject to } & \mathbf{A}\mathbf{x} = \mathbf{b}, \\ & \text{lb} \leq \mathbf{x} \leq \text{ub}, \end{aligned} \tag{7.4}$$

where $\mathbf{I}$ is identity matrix of appropriate size and lb and ub are lower and upper bounds for elements of $\mathbf{x}$. To solve such optimization problem *quadprog* and *lsqlin* functions can be used.

7.3.4 Controling multiple particles

The proposed control scheme is also capable of controling multiple particles. The system of linear equations solved would remain the same, only the elements $\mathbf{A}$ and $\mathbf{b}$ of (7.3) would change. Since we are going to use the same number of microchannels n for control, unknown vector $\mathbf{x}$ remains the same. For m microobjects to control we now have

$$\mathbf{A} = \begin{pmatrix} u_{1,1} & u_{1,2} & \dots & u_{1,n} \\ v_{1,1} & v_{1,2} & \dots & v_{1,n} \\ w_{1,1} & w_{1,2} & \dots & w_{1,n} \\ u_{2,1} & u_{2,2} & \dots & u_{2,n} \\ v_{2,1} & v_{2,2} & \dots & v_{2,n} \\ w_{2,1} & w_{2,2} & \dots & w_{2,n} \\ \dots & \dots & \dots & \dots \\ u_{m,1} & u_{m,2} & \dots & u_{m,n} \\ v_{m,1} & v_{m,2} & \dots & v_{m,n} \\ w_{m,1} & w_{m,2} & \dots & w_{m,n} \end{pmatrix}, \tag{7.5}$$

where the first subindex of u, v, and w stands for the order number of considered microobject. So we have to evaluate velocity vector at positions of all the manipulated microobjects. Vector **b** changes in the same manner

$$\mathbf{b} = K(\mathbf{p}_{\mathrm{DES}} - \mathbf{p}) = K \left(\begin{pmatrix} x_{1,\mathrm{des}} \\ y_{1,\mathrm{des}} \\ z_{1,\mathrm{des}} \\ x_{2,\mathrm{des}} \\ y_{2,\mathrm{des}} \\ z_{2,\mathrm{des}} \\ \dots \\ x_{m,\mathrm{des}} \\ y_{m,\mathrm{des}} \\ z_{m,\mathrm{des}} \end{pmatrix} - \begin{pmatrix} x_1 \\ y_1 \\ z_1 \\ x_2 \\ y_2 \\ z_2 \\ \dots \\ x_m \\ y_m \\ z_m \end{pmatrix} \right), \tag{7.6}$$

7.3.5 6-way valve

With the geometry described we can, of course, control the microchannels as such we do have a 6-way valve. We would just put our points in which **A** and **b** are computed into the centers of the channels (the velocity profile is the same in the whole microchannel thanks to the continuity law). If we would like to control only one microchannel flow, it would be the sum of all inlet velocity flows from the other microchannels.

Also, this control approach is easily expandable when we would like to use a different number of connected microchannels. The only thing changing would be the sizes of **A** and **x**.

7.3.6 Electroosmosis involvement

At this point one may ask how to control fluid flow in this setting with electroosmosis. The answer is simple, we would control the fluid flow through microchannels with electrodes at the bottom boundary. Such geometry with 50 μm electrodes is shown in fig. 7.8

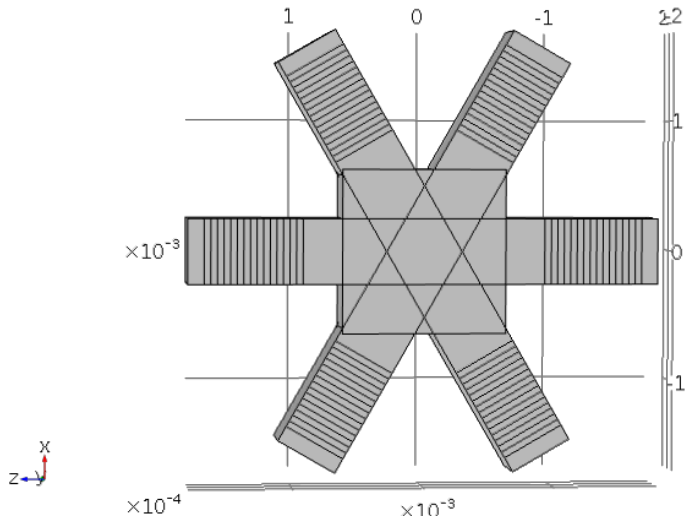

Figure 7.8. Control domain design with electrodes on the bottom surface.

If the microchannels are not extremely large in height and width dimensions the fluid flow induced by electroosmosis does set the whole bulk of fluid to motion. Now we

create a FEM model of one of the microchannels to compute the dependency between the applied potential frequency and amplitude and created pumping flow speed. For speeding up the computations a 2D model of the microchannel was used. This reduction is based on the fact the length of the microchannel is much larger than its height and width. The relationship between potential amplitude (with fixed frequency $f = 100$ Hz) and average pumping velocity and inlet velocity profile is shown in fig. 7.9.

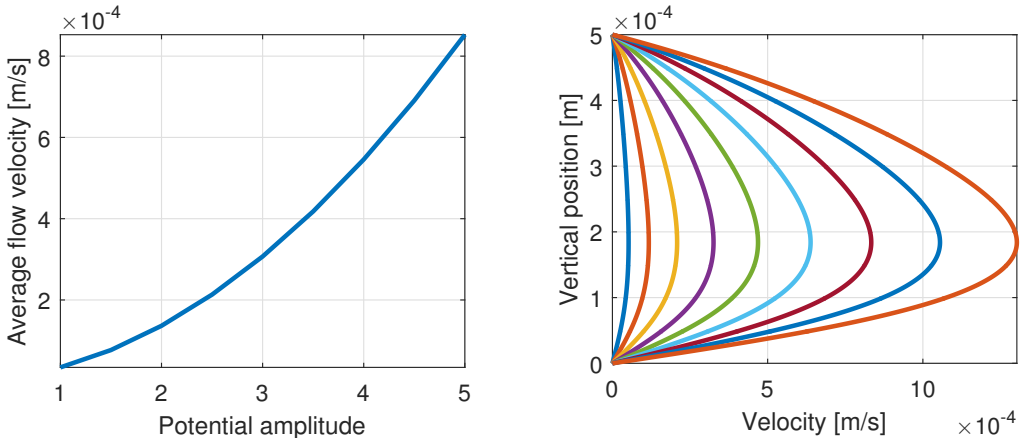

Figure 7.9. Dependancy of pumping velocity and inlet/outlet flow profile on traveling potential wave amplitude. The velocity profile curves (b) are generated from the same data presented in (a) and can be matched.

7.3.7 Simulations

The proposed control model was numerically simulated using the time-stepping method and it proved it could manipulate 1 and 2 particles independently in a 2D plane using fluid flow control. The results are presented in fig. 7.10. Only a center part of the geometry 7.8 is shown.

For time reasons, both simulations were done by directly setting the microchannels' inlet average velocities rather than setting the electrode potentials. The numerical simulations are then much faster since by far sparser FEM geometry mesh is needed. The average inlet velocities are proportional to a particular potential set to the electrode array as shown in fig. 7.9. This was verified by a simulation. There is only a slightly different shape of the velocity field at the boundaries of the considered microchannel. It was observed experimentally, electroosmotically driven fluid flow velocity peaks at a slightly lower vertical position than a classic hydrodynamical microchannel flow.

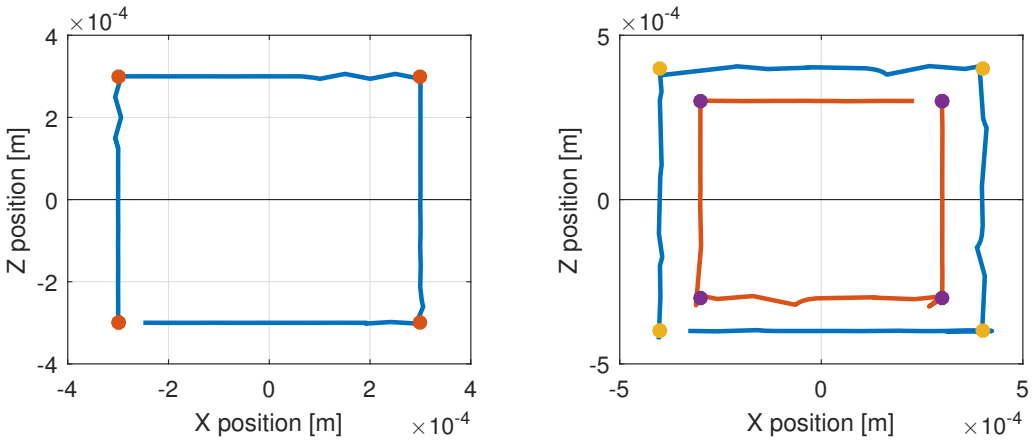

Figure 7.10. Manipulation with (a) one particle, (b) two particles. The curves represent particles trajectories, points are waypoints.

Chapter 8
Future work proposals

In this chapter, I will briefly introduce two ideas for future works based on this thesis.

8.1 Green's function modeling

In general two problems have to be solved by FEM while treating electroosmosis – electrical and hydromechanical problems. These computations are costly and we could benefit from replacing at least one of them with an easier way of computation, especially when we are not interested in a solution in the whole liquid bulk – for example when trying to control the movement of a single or a few particles.

Significantly faster and less computer power intensive solution would be to compute fluid flow at certain points of a predefined computational domain by used a so-called Green's function. A Green's function in its simpler explanation is a spatial impulse response for a point source. Considering a computational domain with boundary conditions defined all over its boundaries a solution at an arbitrary point inside the domain can be acquired by taking a convolution of G, the Green's function, with the boundary condition h. In 1D case, we would have

$$u(x) = \int_{-\infty}^{\infty} h(x')G(x - x')dx'. \tag{8.1}$$

Getting the function G is a non-trivial task. Fortunately, a rule for G is known for a point source. It is called a Stokeslet [15] and it can model an impulse response for Stokes equation (4.5) which is a linearized version of Navier-Stokes equation since linearity is a necessary precondition for the use of Green's function modeling approach.

Now to model the electroosmotic fluid flow inside the fluid bulk we need to model the boundary conditions as a combination of Stokeslets over the electrodes and zero fluid flows over other boundaries. This approach was however not pursued further and I leave it only as an idea for future development of this thesis. For anyone interested in modeling fluid flows using Green's function, bare basics can be also found in [15] and regarding more in-depth literature these books are recommended by the community [42], [43], [44] and [45].

8.2 Another take on DC electroosmosis

Towards the end of work on my thesis I encountered an interesting research paper [41]. In this paper, the authors describe a control system based on a DC electroosmosis and despite all the other papers I found they use a DC electroosmotic effect induced by a voltage significantly lower (1-10 V) than in all other works presented by the community (order of kilovolts for traditional electroosmosis).

The authors show they can independently steer multiple yeast cells and bacteria (of diameter about 5 μm) as well as so-called quantum dots particles (of diameter less than

1 µm) inside a domain consisting of 2 to 4 crossing microchannels. The dimensions of the fabricated area in which the particles are controlled is far beyond reach of production we are capable of making at Department of Control Engineering at CTU right now. The height of the fluid filled channels was only 10µm. And a width of the microchannels was about 50 µm.

To fabricate such a structure a photolithography technique as explained in chapter 5 can be used. The fabricated structure is then covered in PDMS polymer to create the desired microchannel as shown in figure 8.1. Even though the PDMS is more or less see through, the microscope or camera should be placed under the structed to view it from below, because it is easier to focus at such small particles through glass than through PDMS.

The control procedure is already tested on a mathematical model in section 7.3.

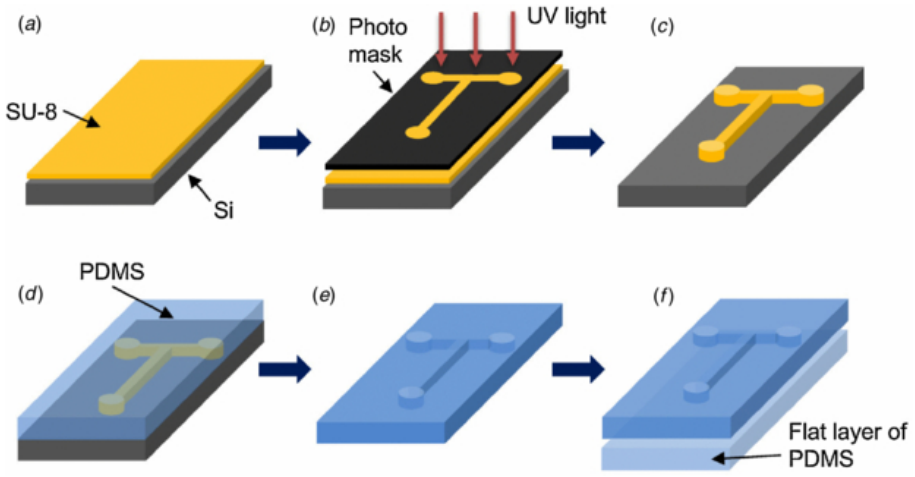

Figure 8.1. PDMS microchannel fabrication outline. The image is reprinted from [46].

8.3 Following this thesis

For anyone who would like to take on where I finished. I would suggest the next step would be to make the experiments more consistent. The first step to do would be to try to lower the volume of fluid operated with and also try move it in closed volume – without the free access to the fluid pool from above.

That would actually mean to stop using the PDMS pools and move to a closed structure fabricated with the same procedure as shown in 8.1. Inside this closed volume, the fluid would be brought from two small reservoirs right next to it, those reservoirs might have a free access from above to actually put some fluid inside the closed volume over the electrodes.

In my experiments, the water column height had to be at minimum around 1.5 mm. This was given by the usage of PDMS pools which were not closed. To deploy smaller amounts of water into the PDMS pool the PDMS itself should be treated. For example, an oxygen plasma treatment causes the PDMS material to reduce its hydrophobicity.

Chapter 9
Conclusions

In this thesis, electroosmosis as means of flow control mechanism has been studied. We began with introducing the basic concepts followed by providing a mathematical model implemented in a commercial finite element method solver. Five different functional microelectrode arrays were produced to perform various experiments to validate the model. In the end, three control strategies were proposed and tested on the mathematical model created.

Unfortunately, the experimental part did not go very well. The electroosmotic motion was observed, but it proved to be unreliable in terms of repeatability. Sometimes no motion was detected at all even while using the same microelectrode array for which fluid flow was observed before with the same input potential properties. The exact reasons why did we observe this chaotic nature of the experiments were, however, not determined. This is the main setback encountered.

I conclude the mathematical model matches the observations at least in predicted trajectories of tracer particles. Also, knowledge and new experiences in microelectrode arrays fabrication were acquired and documented, which might help in future works in the field of micromanipulation done at Department of Control Engineering. A detailed instruction manual for maskless photolithography was created.

The proposed control approaches did work well with the mathematical model. A real system test of these methods is held back by the problems with the experiments and a lack of greater know-how in PDMS structures fabrication.

Hopefully, this thesis will help anyone who would also like to take the challenge of getting an electroosmotic fluid flow control system to work.

References

[1] Hywel Morgan, and Nicolas G Green. *AC electrokinetics: colloids and nanoparticles*. Research Studies Press, 2003.

[2] Herbert H Woodson, and James R Melcher. Electromechanical dynamics. 1968,

[3] Lingxin Chen, Hailong Wang, Jiping Ma, Chengxia Wang, and Yafeng Guan. Fabrication and characterization of a multi-stage electroosmotic pump for liquid delivery. *Sensors and Actuators B: Chemical*. 2005, 104 (1), 117–123.

[4] Luca Ribetto. *Microfabricated All-Around-Electrode AC Electro-osmotic Micropump*. Ph.D. Thesis, Citeseer. 2012.

[5] Daniel J Laser, and Juan G Santiago. A review of micropumps. *Journal of micromechanics and microengineering*. 2004, 14 (6), R35.

[6] Antonio Ramos, Hywel Morgan, Nicolas G Green, and A Castellanos. Ac electrokinetics: a review of forces in microelectrode structures. *Journal of Physics D: Applied Physics*. 1998, 31 (18), 2338.

[7] Sophie Loire, Paul Kauffmann, I Mezić, and CD Meinhart. A theoretical and experimental study of ac electrothermal flows. *Journal of Physics D: Applied Physics*. 2012, 45 (18), 185301.

[8] Ivan R Perch-Nielsen, Nicolas G Green, and Anders Wolff. Numerical simulation of travelling wave induced electrothermal fluid flow. *Journal of Physics D: Applied Physics*. 2004, 37 (16), 2323.

[9] Nicolas G Green, Antonio Ramos, Antonio Gonzalez, Antonio Castellanos, and Hywel Morgan. Electrothermally induced fluid flow on microelectrodes. *Journal of Electrostatics*. 2001, 53 (2), 71–87.

[10] Nicolas G Green, Antonio Ramos, Antonio González, Hywel Morgan, and Antonio Castellanos. Fluid flow induced by nonuniform ac electric fields in electrolytes on microelectrodes. I. Experimental measurements. *Physical review E*. 2000, 61 (4), 4011.

[11] Antonio González, Antonio Ramos, Nicolas G Green, Antonio Castellanos, and Hywel Morgan. Fluid flow induced by nonuniform ac electric fields in electrolytes on microelectrodes. II. A linear double-layer analysis. *Physical review E*. 2000, 61 (4), 4019.

[12] Nicolas G Green, Antonio Ramos, Antonio Gonzalez, Hywel Morgan, and Antonio Castellanos. Fluid flow induced by nonuniform ac electric fields in electrolytes on microelectrodes. III. Observation of streamlines and numerical simulation. *Physical review E*. 2002, 66 (2), 026305.

[13] Pablo García-Sánchez, Antonio Ramos, Nicolas G Green, and Hywel Morgan. Experiments on AC electrokinetic pumping of liquids using arrays of microelectrodes. *IEEE Transactions on Dielectrics and Electrical Insulation*. 2006, 13 (3), 670–677.

[14] Antonio Ramos, Hywel Morgan, Nicolas G Green, Antonio González, and Antonio Castellanos. Pumping of liquids with traveling-wave electroosmosis. *Journal of Applied Physics*. 2005, 97 (8), 084906.

[15] Brian J Kirby. *Micro-and nanoscale fluid mechanics: transport in microfluidic devices*. Cambridge University Press, 2010.

[16] M Mpholo, CG Smith, and ABD Brown. Low voltage plug flow pumping using anisotropic electrode arrays. *Sensors and Actuators B: Chemical*. 2003, 92 (3), 262–268.

[17] Shiang-Chi Lin, Jau-Ching Lu, Yu-Lung Sung, Chih-Ting Lin, and Yi-Chung Tung. A low sample volume particle separation device with electrokinetic pumping based on circular travelling-wave electroosmosis. *Lab on a Chip*. 2013, 13 (15), 3082–3089.

[18] Petr Červenka, Michal Přibyl, and Dalimil Šnita. Numerical study on AC electroosmosis in microfluidic channels. *Microelectronic engineering*. 2009, 86 (4), 1333–1336.

[19] Jiří Hrdlička, Petr Červenka, Michal Přibyl, and Dalimil Šnita. Mathematical modeling of ac electroosmosis in microfluidic and nanofluidic chips using equilibrium and non-equilibrium approaches. *Journal of Applied Electrochemistry*. 2010, 40 (5), 967–980.

[20] Jiří Hrdlicka, Petr Cervenka, Tomáš Jindra, Michal Pribyl, and Dalimil Snita. Mathematical modeling of traveling wave micropumps: Analysis of energy transformation. *IEEE Transactions on Industry Applications*. 2013, 49 (2), 685–690.

[21] ABD Brown, CG Smith, and AR Rennie. Pumping of water with ac electric fields applied to asymmetric pairs of microelectrodes. *Physical review E*. 2000, 63 (1), 016305.

[22] Brian P Cahill, Laura J Heyderman, Jens Gobrecht, and Andreas Stemmer. Electro-osmotic streaming on application of traveling-wave electric fields. *Physical review E*. 2004, 70 (3), 036305.

[23] Hukun Yang, Hongyuan Jiang, Dong Shang, Antonio Ramos, and Pablo Garcia-Sanchez. Experiments on traveling-wave electroosmosis: effect of electrolyte conductivity. *IEEE Transactions on Dielectrics and Electrical Insulation*. 2009, 16 (2), 417–423.

[24] Pablo García-Sánchez, Antonio Ramos, Nicolas G Green, and Hywel Morgan. Traveling-wave electrokinetic micropumps: Velocity, electrical current, and impedance measurements. *Langmuir*. 2008, 24 (17), 9361–9369.

[25] Brian Patrick Cahill. *AC electro-osmotic pumping for microfluidic systems*. Ph.D. Thesis, Eidgenössische Technische Hochschule ETH Zürich, Nr. 15856. 2005.

[26] Ping Wang, Zilin Chen, and Hsueh-Chia Chang. A new electro-osmotic pump based on silica monoliths. *Sensors and Actuators B: Chemical*. 2006, 113 (1), 500–509.

[27] Martin Z Bazant, and Yuxing Ben. Theoretical prediction of fast 3D AC electroosmotic pumps. *Lab on a Chip*. 2006, 6 (11), 1455–1461.

[28] Pablo García S'anchez. *Travelling-wave electrokinetic micropumps*. Ph.D. Thesis, Universidad of Sevilla. 2008.

[29] Tomáš Michálek. Maticové elektrodové pole pro dielektroforézu - základní řízení polohy. *Bakalářská práce*. ČVUT v Praze, 2013,

[30] Tomáš Michálek. *Real-time optimization-based control for dielectrophoresis*. Master's Thesis, CTU in Prague. Czech Republic, 2013.

[31] Jakub Drs. *Micromanipulation platform for droplets*. Master's Thesis, CTU in Prague. Czech Republic, 2015.

[32] Antonio Castellanos, Antonio Ramos, Antonio Gonzalez, Nicolas G Green, and Hywel Morgan. Electrohydrodynamics and dielectrophoresis in microsystems: scaling laws. *Journal of Physics D: Applied Physics*. 2003, 36 (20), 2584.

[33] *Building Virtual Models in Engineering An Introduction to Finite Elements*. `http://ta.twi.tudelft.nl/nw/users/domenico/intro_fem/intro_fem.pdf`. Accessed: 2016-12-04.

[34] Neophytos Loucaides, Antonio Ramos, and George E Georghiou. Novel systems for configurable AC electroosmotic pumping. *Microfluidics and Nanofluidics*. 2007, 3 (6), 709–714.

[35] Nazmul Islam, and Jie Wu. *Microfluidic transport by AC electroosmosis*. In: *Journal of Physics: Conference Series*. 2006. 356.

[36] Jie Wu, Yuxing Ben, David Battigelli, and Hsueh-Chia Chang. Long-range AC electroosmotic trapping and detection of bioparticles. *Industrial & engineering chemistry research*. 2005, 44 (8), 2815–2822.

[37] Marek Záveský. *Příprava a charakterizace tištěných elektronických struktur* . Master's Thesis, CTU in Prague. Czech Republic, 2016.

[38] Timothy A Fofonoff, Sylvain M Martel, Nicholas G Hatsopoulos, John P Donoghue, and Ian W Hunter. Microelectrode array fabrication by electrical discharge machining and chemical etching. *IEEE transactions on biomedical engineering*. 2004, 51 (6), 890–895.

[39] Jakub Drs. Čtyřsektorové elektrodové pole pro dielektroforézu. *Bakalářská práce*. 2012,

[40] Jiří Zemánek. *Noncontact parallel manipulation with micro- and mesoscale objects using dielectrophoresis*. Master's Thesis, Prague, Czech Republic, 2009.

[41] Roland Probst, Zachary Cummins, Chad Ropp, Edo Waks, and Benjamin Shapiro. Flow control of small objects on chip: Manipulating live cells, quantum dots, and nanowires. *IEEE Control Systems*. 2012, 32 (2), 26–53.

[42] Ivar Stakgold, and Michael J Holst. *Green's functions and boundary value problems*. John Wiley & Sons, 2011.

[43] Dean G Duffy. *Greens functions with applications*. CRC Press, 2015.

[44] Mark S Gockenbach. *Partial differential equations: analytical and numerical methods*. Siam, 2010.

[45] Michael Shearer, and Rachel Levy. *Partial Differential Equations: An Introduction to Theory and Applications*. Princeton University Press, 2015.

[46] Jihoon Lee, Jungwoo Kim, Hyoungsub Kim, Young Min Bae, Kyeong-Hee Lee, and Hyoung J Cho. Effect of thermal treatment on the chemical resistance of polydimethylsiloxane for microfluidic devices. *Journal of Micromechanics and Microengineering*. 2013, 23 (3), 035007.

Appendix A
Maskless photolithography instruction manual

The following instructions would lead the reader in fabricating a gold conductive structure on a glass substrate.

1. Clean the glass substrate (with 50 nm of NiCr and 150 nm of Au already deposited) with acetone and/or isopropyl alcohol to remove grease and large dust and dirt particles.
2. To remove as much dust as possible put the substrate in sonic bath for about 5 minutes.
3. Dry the sample completely using compressed air.
4. Put the sample to spincoater and deposit negative photoresist ma-N 1410 (made by Micro resist technology GmbH) j evenly.
5. Spincoat at 3000 rpm for 30 sec.
6. Bake the sample at 100°C.
7. Load the sample to Durham Magneto Optics MicroWriter ML3 direct-write photolithography machine.
8. Do the calibration procedure it the control PC program.
9. Load the .cif layout design into the control PC program.
10. Start the writing and wait (the process usually takes coupe of hours for one substrate).
11. After the writing is finished remove the sample and develop the photoresist in ma-D 533/S (made by Micro resist technology GmbH) developing solution, the development should take about 30-40 seconds, clean the sample with water immediately after taking it from the developing solution – water will stop the reaction. It is possible to exaine the sample under the microscope and see the light reflections over the sample. After multiple fabrication processes one can distinguish between gold covered in photoresist and not covered. If there are spots where there is still photoresist over the gold which should be removed, the developing process can repeated for shorter period of time.
12. Bake the sample for 8 minutes at 140°C.
13. Etch the gold not covered by the photoresist with aqua regia (HNO_3 +3 HCl – a 1:3 mixture of nitric acid and hydrochloric acid) solution. This process takes anywhere between 15 to 35 seconds depending on the state of gold and the photoresist. The process is visble by eye. Do not etch the sample for any time longer than necessary, because the aqua regia can attack even the gold covered by the photoresist). Again, after taking the sample out of aqua regia, dip it into water and rinse to stop the reaction. The etching process is quite fast and dangerous. When overetching the sample the small scale structures in the design can get ruined very quickly. There is also a second possible solution for etching the gold away. It is 1:4:40 mixture of I_2:KI:H_20. Etching in this mixture takes much more time (even 5 minutes).
14. Etch the chromium away with diamonium hexanitratocerate for about 30 seconds. Again the process is visible by eye.
15. The remaining photoresist can be washed away with acetone.

Appendix B
Getting the Allied Vision Pike camera working in MATLAB

Because it was not really straightforward to get the Allied Vision Pike camera mounted on a microscope to get working in MATLAB environment, I present a short guide of how to do it for anyone who would like to follow my work. Even though the final process is simple, documentation for the camera is missing (Pike camera is no longer offered in the company's store) from the internet and this guide had to be done together with the support from Allied Vision company.

There are multiple driver packeges for the camera. If you have installed the AVT Universal driver package, you can see the camera preview, save the camera image and record video using UniCam viewer which was installed with the AVT Universal driver. If you do not need any more functionality than this, you can stop reading now.

This software package is however obsolete and does not work with MATLAB Image Acquisition toolbox. This toolbox is necessary to have for getting the images from camera to MATLAB.

To get the camera working you have to uninstall the AVT Universal driver and install Vimba software from Allied Vision website. It is necessary to really uninstall the Universal driver. Now one has to install GenICam Inteface and GigE Vision Hardware support packeges in MATLAB (Home — Add-Ons — Get Hardware Support packages).

Run MATLAB command *imaqhwinfo* to see if there is *gentl* adaptor listed. If there is, run command *imaqhwinfo('gentl')* to verify MATLAB does see your Pike camera device. Now the camera is ready to use in MATLAB/Simulink. The easiest way to verify is to create a new Simulink model and place a *From Video Device* and *Video Viewer* blocks or clicking the *From Video Device* block preview button.

Programatically preview the camera image with this two commands

```
vid = videoinput('gentl',1);
preview(vid);
```

If you prefer to use the AVT UniCam viewer over recording the video in MATLAB it needs the old drivers to work, so MATLAB connectivity will not be functional again. One has to choose which way is more comfortable for him or her.

Appendix C
Microfabrication possibilities and contacts

In this appendix, I would like to present all the possibilities in performing the microelectrode fabrication steps outside of the research group AA4CC, which I was part of when working on this thesis. Names of people which the price, free time, etc. negotiations should be made with at the individual facilities are also included. This list might especially get handy if someone would like to follow my work in the next semester or the next academic year. Please be aware of the fact information in this appendix might get out of date after printing this thesis.

C.1 Substrate coating

- Department of Advanced Materials

  There is a possibility to get glass substrates coated at Department of Advanced Materials of Department of Control Engineering of Czech Technical University in Prague. Right now, only copper sputter coating targets are available. If we would provide gold and chromium targets of our own, we could use their sputtering machine. The price of these targets is in order of tens of thousands Czech crowns.

  Contant persons are: prof. Ing. Tomáš Polcar Ph.D. and Ing. Martin Daněk.
- Thin Film Technological Service (TTS s.r.o)

  TTS is a commercial company offering various options in thin layer depositions. 30x30 cm area of 50nm NiCR and 150nm Au costs about 200 CHF. Depending on current ratio it is about 2600 CZK. Gold coated glass substrates used in this thesis were acquired from this Prague company.

  Contact person: Ing. Vítězslav Lamač
- Institute of Physics of the Czech Academy of Sciences (Cukrovarnicka)

  At Institute of Physics of the Czech Academy of Sciences on Cukravarnicka in Prague both ITO and chrome/gold depositions can be done.

  Contact person: Ing. Martin Müller

C.2 Maskless photolithography

- University of West Bohemia

  At University of West Bohemia, there is a possibility to perform photolithography using gold coated substrates, which we need to deliver ourselves. The fabrication resolution should be in order of 1 to 5 microns. Also, trials with copper coated substrates can be done.

  Contact person: Ing. Miloš Svoboda, Ph.D.
- Institute of Physics of the Czech Academy of Sciences (Slovanka)

  This is the place I got the coated substrates processed. Again the fabrication resolution is about 5 microns. I delivered the gold coated substrates myself.

Contact person: Ing. Ján Lančok, Ph.D.

- The Institute of Photonics and Electronics of the Czech Academy of Sciences

  Starting from February 2017, there is a new maskless photolithography machine deployed to yet another instituion of the The Institute of Photonics and Electronics of the Czech Academy of Sciences.

  Contant person: Ing. Michal Cifra, Ph.D.
- Tesla Blatná a.s.

  In this commercial company even small-scale production photolithography is possible. Delivering a few samples on gold coated substrates costs about 12 000 CZK.

  Contact person: Margita Ozaňáková

C.3 Institude of Analytical Chemistry of the Czech Academy of Sciences (Brno)

A research group around Ing. František Foret, CSc., is a research partner of AA4CC research group at Czech Technical University in Prague. Both coating (chromium and gold) and maskless photolithography can be done there. However during work on my thesis, the maskless photolithography machine they use was not working properly and had to be sent to Germany.

Contac person: Ing. František Foret, CSc.

Appendix D
Abbreviations

CTU	Czech Technical University in Prague
DCE	Department of Conrol Engineering
DI water	Deionized water
ITO	Indium tin oxide
FEM	Finite element method
PDE	Partial differential equation
PIV	Particle image velocimetry
UV	Ultra violet (light)
μTAS	Micro total analysis system

Appendix E
List of symbols

$\mathbf{a}$	Particle acceleration vector
A	Matrix of system of linear equations
b	Right hand side of system of linear equations
c	Chemical species concentration
C_d	Diffuse layer capacitance
C_{DL}	Double layer capacitance
C_s	Stern layer capacitance
D	Diffusivity
$\mathbf{D}$	Electric displacement field
$\mathbf{E}$	Electric field
$\mathbf{f}$	External force
$\mathbf{F}$	Force
f	Frequency
$\mathbf{g}$	Gravitational acceleration
i	Complex unit
j	Order index
$\mathbf{I}$	Identity matrix
k_B	Boltzmann constant
K	Scaling constant
L	Characteristic length of a system
p	Pressure
q	Ionic charge
r	Particle radius
Re	Reynolds number
t	Time
$\mathbf{u}$	Fluid velocity vector
$\mathbf{v}$	Particle velocity vector
V	Electrical potential amplitude
x	2D horizontal coordinate
y	2D vertical coordinate
z	Chemical species valence
ε	Permittivity
ε_0	Permittivity of free space
ε^*	Complex permittivity
η	Dynamic viscosity
φ	Electrical potential
φ_0	Electrical potential applied to the electrodes
κ	Reciprocal Debye length ($\kappa = \frac{1}{\lambda_D}$)
λ_D	Debye length
Λ	Ration between Stern and diffuse layer capacitance
σ	Electrical conductivity

ρ	Fluid density
ρ_E	Electric charge density
ω	Angular frequency
ω_r	Charge relaxation frequency
Ω	Non-dimensional frequency